



Bayesian estimations of orientation distribution functions from small-angle scattering enable direct prediction of mechanical stress in anisotropic materials

Patrick T. Corona,¹ Kevin S. Silmore,² Raymond Adkins³,,³ Christian Lang,⁴ Minne Paul Lettinga,^{5,6} James W. Swan,² L. Gary Leal,¹ and Matthew E. Helgeson^{1,*}

¹University of California, Santa Barbara, Department of Chemical Engineering, Santa Barbara, California 93106, USA

²Massachusetts Institute of Technology, Department of Chemical Engineering, Cambridge, Massachusetts 02139, USA

³University of California, Santa Barbara, Department of Physics, Santa Barbara, California 93106, USA

⁴Jülich Centre for Neutron Science, Heinz Maier-Leibnitz Zentrum, D-85747 Garching, Germany

⁵ICS-3, Institut für Weiche Materie, Forschungszentrum Jülich, D-52425 Jülich, Germany

⁶Laboratory for Soft Matter and Biophysics, KU Leuven, Celestijnenlaan 200D, B-3001 Leuven, Belgium



(Received 21 January 2021; accepted 19 May 2021; published 8 June 2021)

Properties of soft materials are influenced by their anisotropic structuring under nonequilibrium fields. Although anisotropic structure-property relationships have been extensively explored theoretically, comparison to experiments requires determination of the microstructural orientation probability distribution function (OPDF) of microstructural elements. Small angle scattering (SAS) measurements encode information about the OPDF, but tools to navigate this connection are incomplete. Here, we develop and validate an explicit framework to link arbitrary OPDFs to SAS measurements. Specifically, we propose, validate, and apply a method, maximum *a posteriori* scattering inference (MAPSI), whereby the OPDF may be obtained from SAS measurements using a Bayesian estimation method. Using this method, we obtain estimates of the full 3D OPDF for two model semidilute fd-virus (rodlike) dispersions at concentrations that are approximately equal to and twice the overlap concentration. From the OPDF, we calculate its second and fourth moments and compare these to predictions for a dilute suspension of rigid rods and to a recent theory for semidilute suspensions. Finally, we use both the theoretical and measured moments to calculate the stress, both for dilute and semidilute suspensions. These predictions are not only compared to each other, but also to measured values of the shear stress, and point to new insights into the behavior of suspensions of highly elongated particles in the transition between dilute and semidilute behavior. We also use this new framework to provide perspective on the connection between scalar parameterizations of scattering and the OPDF that have frequently been used in the past. The new tools developed in this work provide an unprecedented path toward experimental validation of dynamical theories of rodlike colloids and polymers, and for measurement of nonequilibrium structures and stresses of other complex fluids and soft materials with SAS.

DOI: [10.1103/PhysRevMaterials.5.065601](https://doi.org/10.1103/PhysRevMaterials.5.065601)

I. INTRODUCTION

Nonequilibrium fields often produce anisotropic structures and properties in soft materials due to the orientable nature of material elements [1,2]. In such situations, diffraction represents a powerful technique for measuring anisotropic microstructure to connect theoretical models to macroscopic properties. In particular, small angle scattering (SAS) of light or neutrons enables one to probe length scales ranging from nanometers to microns, corresponding to structural features that are relevant to many soft materials [3]. SAS sample environments have been developed to make measurements *in situ* under applied flow, magnetic and electrical fields where the external field can induce microstructural orientation, stretching and/or aggregation [4–8]. Such experiments can be utilized to connect nonequilibrium processing to structure, dynamics and the resultant materials properties of soft material systems [9–11].

In this work, we are specifically concerned with the problem of using SAS to determine the orientation probability distribution function (OPDF) for dispersions of rigid, non-spherical objects under simple shear flow. Although here we focus exclusively on shear flow, the models and methods we discuss can be generalized to other orienting fields. The OPDF describes the probability that a particle will be oriented in a particular direction, and moments of the OPDF provide a direct link to theories that describe structure-property relationships in anisotropic materials, such as mechanical, optical and transport properties [12]. The problem of extracting OPDFs from SAS measurements has received considerable attention [4,6,13,14]. In the following, we will briefly summarize current methods to analyze anisotropic scattering from soft materials, which will highlight the need for new methodology to extract quantitative OPDFs. We refer the interested reader to Ref. [15] for a more thorough review on this subject.

In principle, SAS measurements encode information about the underlying OPDF of the material under measurement. However, in addition to being pre-ensemble averaged, this

*Helgeson@ucsb.edu

information is convoluted by the fact that the OPDF is an intrinsically 3D property (i.e., it can be defined on the surface of a unit sphere representing orientation space for axisymmetric particles), whereas SAS measurements are typically recorded as a 2D projection of the scattering onto a planar detector. In some cases, such as for spatially homogeneous uniaxial fields, symmetry conditions can be imposed to eliminate the need for 3D information from the 2D measurement [16]. By contrast, the most widely utilized flow for studies of soft materials and complex fluids is simple shear flow, which breaks uniaxial symmetry such that a full 3D description is required for the OPDF. As such, there is no exact mapping of the “inverse problem” that connects a single 2D scattering measurement to a unique 3D OPDF. To overcome this limitation, it has been suggested that scattering measurements should be made under a series of rotational 2D projections, however sample environments to make these measurements have not yet been developed [17–19]. In this work, we will explore the use of scattering data in two or three orthogonal planes, as these configurations are currently available for flow-SANS measurements [4,20,21].

In general, prior researchers attempted one of two approaches to estimate the OPDF: (1) the use of various model-free parameterizations of the scattering anisotropy in the measurement plane, which are assumed to correlate with analogous metrics of the real-space 3D OPDF, or (2) the use of a 3D structural model whose predicted scattering is used to fit various parameters of the model to the data. For case (1), scalar parameters such as the “alignment factor” (A_f) and Hermans’ orientation parameter are used to qualitatively track the evolution of SAS anisotropy, and proposals have been made about the relationship of these parameters and moments of the OPDF [13,22–26]. In the SI, we explore this case further, and demonstrate that it does not generally provide quantitative results for moments of the OPDF. For case (2), fitting of SAS patterns has been restricted to situations where the microstructure is modeled as a cylinder and the OPDF is assumed to be uniaxial [14,27–35]. As will be discussed in detail later, the *ill-posedness* of the underlying fitting problem makes these schemes highly sensitive to experimental noise.

Experimental measurement of the OPDFs of nonspherical particles in flow is especially relevant to the development of rheological models of dispersions, nanocomposites and rodlike polymers. For the limiting case of noninteracting, rigid, axisymmetric particles in a Newtonian solvent, a rigorous micromechanical theory for the particle contribution to the stress exists [12,36] based upon evolution of the OPDF according to the Smoluchowski equation in orientation space where orientational probability is advected by flow (as described by Jeffery’s equation [37]) and randomized by rotational diffusion due to thermal fluctuations. Corrections to this theory have been proposed for semidilute systems to account for direct particle interactions [38–40]. In all of these theories, the structure and stress are only dependent on the particle shape, concentration, and moments of the OPDF [12]. Therefore direct measurement of the OPDF under flow would provide a critical test of the theoretical models for particle orientation, and would also enable a direct prediction of the stress that can be compared with experimental measurements. While

the OPDFs of micron-sized particles can be directly probed with optical microscopy, scattering techniques such as SAS are required to probe the OPDF of nanoparticles under flow [41–43]. Given the practical ability to produce homogeneous simple shear flows and the aforementioned breaking of uniaxial symmetry, simple shear flow presents a rigorous test of such theories. The preferred model system for structural and mechanical studies of nonspherical nanoparticles in simple shear flow has been aqueous dispersions of fd-viruses—rigid, monodisperse and rodlike particles [26,44–48]. In this work, we will probe SAS from aqueous dispersions of fd-virus particles in simple shear flow.

The primary objectives of this work are the following. (1) First, to develop a generalized framework for analyzing anisotropic SAS measurements of dispersions of rodlike particles under simple shear flow that accounts for contributions to the scattering resulting from particle shape and the 3D nature of the OPDF, ultimately resulting in parameter-free and fully 3D OPDF estimations from multiprojection SAS measurements. (2) Second, to utilize this method to compare measured properties of the fd-virus dispersions at concentrations near or somewhat above the critical overlap concentration ϕ^* , including moments of the OPDF, and rheological properties in shear flow, with theoretical predictions for dilute suspensions, and extensions to that theory that have been proposed for semidilute systems.

With regard to the first objective, we develop the expressions for predicting the scattering due to oriented, nonspherical particles in a dilute dispersion under simple shear flow and propose model-independent methods to extract the OPDF from SAS measurements that account for the three-dimensionality of particle orientations. We then develop a new approach based upon Bayesian estimation theory that we call “maximum *a posteriori* scattering inference” (MAPSI) to extract parameter-free estimates of the 3D OPDF from planar SAS measurements. We test the accuracy and properties of this method by applying it to the case of dilute suspensions where we can calculate the SAS patterns, and for which we know the exact OPDF. We then apply MAPSI to infer OPDFs from SANS measurements of semidilute fd-virus dispersions in simple shear flow. We calculate moments of the OPDF that are related to the macroscopic stress and compare them with moments calculated from the theories for a dilute suspension of noninteracting particles. Using the measured moments, we also calculate the bulk stress, using an expression derived by Batchelor for noninteracting particles [12]. These predictions of the stress are then compared with mechanical measurements of the shear stress for the same fd-virus suspensions as a means to test the applicability of the theoretical expressions for the stress.

A. Experimental methods

The fdY21M viruses used in this work are monodisperse, rodlike (with length, $L = 920$ nm, and radius, $R = 3.3$ nm), and rigid ($L_p/L = 11$, where L_p is the persistence length) particles [26,40,44–47]. The fdY21M viruses were prepared using standard protocols [49]. The viruses were dispersed in a 20 mM Tris/100 mM NaCl/D₂O buffer at two concentrations of 0.1 and 0.2 vol% (where $\phi^* \approx 24(2R/L)^2 = 0.124$ vol%

is the overlap concentration [2]). The salt concentration was chosen to eliminate the effect of charge interactions between the viruses as demonstrated by Lang *et al.* using rheological measurements, and the virus concentrations were chosen to be in the regime of $\phi^* = O(1)$ to explore the effects of interactions between the viruses, while limiting direct physical interactions and still providing sufficient scattering signal above background [40].

Two different flow cells were used to probe different projections of SANS data from the same sample under steady simple shear flow with varying shear rate, $\dot{\gamma}$. Scattering in the flow-vorticity plane was probed utilizing the 1–3 plane rheo-SANS flow cell, which is an Anton Paar MCR 501 rheometer (Anton Paar GmbH, Graz, Austria) with a quartz Couette geometry [20]. Since the 1–3 plane measurements were made in a rheometer, the shear stress was measured simultaneously. Scattering in the flow-gradient plane was probed using a 1–2 plane shear cell [20]. A similar gap size (1 mm) and outer cylinder radius (25 mm) were used for both sample environments. Both measurements were conducted at the National Institute of Standards Center for Neutron Research on the VSANS instrument with $\lambda = 5 \text{ \AA}$ and $\Delta\lambda/\lambda = 0.11$. In this work, we include results for the q -range from 0.02 to 0.2 \AA^{-1} . All measurements were performed at 25 °C. Data from the measurements were reduced using standard NCNR protocols with Igor PRO software to correct for empty cell, background, and intensity normalization to an absolute scale [50].

II. RHEOLOGICAL THEORIES FOR SUSPENSIONS OF BROWNIAN PARTICLES

In the sections to follow, we utilize previously published theories for the rheology of dilute and semidilute suspensions of axisymmetric, elongated Brownian particles. In the interest of brevity, we do not repeat these theories here, but we recognize that they may not be familiar to all readers and we therefore summarize the key aspects in the SI. These theories consist of two parts. One is the theory for calculating the OPDF in flow, namely the Smoluchowski or convection-diffusion equation in orientation space,

$$\frac{DN}{Dt} + \frac{\partial}{\partial \mathbf{p}} \cdot (N\dot{\mathbf{p}}) = \frac{\partial}{\partial \mathbf{p}} \cdot \left(D_r \frac{\partial N}{\partial \mathbf{p}} \right), \quad (1)$$

where $N(\mathbf{p}, t)$ is the OPDF, the unit vector \mathbf{p} specifies the orientation of the axis of particle symmetry, $\dot{\mathbf{p}}$ is the rotation of this axis by the flow, and D_r is the rotational diffusivity. The second component of the theory is the expression that relates the stress to the OPDF.

The only case for which an exact theory is available is the limit of a dilute suspension of noninteracting Brownian particles. For this case,

$$\dot{\mathbf{p}} = \boldsymbol{\Omega} \cdot \mathbf{p} + \frac{r_e^2 - 1}{r_e^2 + 1} [\mathbf{E} \cdot \mathbf{p} - (\mathbf{p} \cdot \mathbf{E} \cdot \mathbf{p})\mathbf{p}], \quad (2)$$

which is Jeffery's solution for rotation of an axisymmetric particle in a homogeneous flow [37].

Here $\boldsymbol{\Omega}$ is the vorticity tensor, \mathbf{E} the rate of strain tensor, and r_e the particle's effective aspect ratio (for cylinders,

$r_e \approx \frac{L}{2R} \sqrt{\frac{8\pi}{16.35 \ln(\frac{L}{2R})}}$ where L is the cylinder length and R is the cylinder radius) [51]. The rotational diffusion coefficient for an isolated Brownian particle is [52]

$$D_r = D_{r,0} = \frac{3k_b T \ln(\frac{L}{R})}{\pi \eta_s L^3} \left(\frac{1 - \frac{1.5}{\ln(\frac{L}{R})}}{1 + \frac{0.64}{\ln(\frac{L}{R})}} \right), \quad (3)$$

where $k_b T$ is the thermal energy and η_s is the suspending fluid viscosity [2,53]. For this limit, there is also an exact framework first provided by Batchelor for calculating the particle contribution to the stress tensor, given knowledge of the OPDF [12]. For highly elongated particles this can be expressed in the form

$$\sigma_p = 2\eta_s \phi \left(A \left(\mathbf{S}^{(4)} : \mathbf{E} - \frac{1}{3} \mathbf{I} \mathbf{S} : \mathbf{E} \right) + D_{r,0} F \left(\mathbf{S} - \frac{1}{3} \mathbf{I} \right) \right), \quad (4)$$

where

$$\mathbf{S} = \int \mathbf{p} \mathbf{p} N(\mathbf{p}, t) d\mathbf{p} \text{ and } \mathbf{S}^{(4)} = \int \mathbf{p} \mathbf{p} \mathbf{p} \mathbf{p} N(\mathbf{p}, t) d\mathbf{p} \quad (5)$$

are the second and fourth moments of the OPDF. Here, ϕ is the volume fraction of rods and A and F are coefficients that depend only on the aspect ratio r_e of the particles. Equation (4) will be referred to as Batchelor's expression for the remainder of this work.

For the simple shear flows considered in this work, the nonzero components of the vorticity and rate of strain tensors are $\Omega_{12} = -\Omega_{21} = \dot{\gamma}/2$ and $E_{12} = E_{21} = \dot{\gamma}/2$, where $\dot{\gamma}$ is the shear rate and the subscripts 1 and 2 denote the flow and gradient directions. Qualitatively, the orientation distribution will depart from the isotropic, equilibrium distribution in a manner that depends on the relative strength of the flow and the rotational diffusion. This can be parameterized via the rotational Peclet number, $Pe_r = \dot{\gamma}/D_{r,0}$. For the fd-virus in D₂O solvent at 25 °C ($\eta_s = 1.1 \text{ mPa s}$), this yields $D_{r,0} = 17 \text{ s}^{-1}$. Therefore we expect to observe significant alignment of the microstructure when $\dot{\gamma} > 17 \text{ s}^{-1}$ (i.e. $Pe_r > 1$). To obtain detailed quantitative results for $N(\mathbf{p}, t)$, the Smoluchowski equation (1) was solved numerically using the method outlined by Férec *et al.*, which was specifically designed to enable higher stability at large Pe_r [54]. The details of this method and the discretization used in the present work can be found in the SI. Calculations of moments of $N(\mathbf{p})$ and scattering intensities, $\overline{I(\mathbf{q})}$, were made using numerical integration with the mid-point rule.

In the present work, we will use the OPDF for the dilute case to both predict the expected SAS patterns and to predict the stress. We will discuss the theory required for predicting the scattering in the next section as it requires some extension of existing theory. The stress is calculated via Eqs. (4) and (5), with geometric parameters $A = 820$, $D_{r,0} = 17 \text{ s}^{-1}$, and $F = 3830$, corresponding to $r_e = 76$, which is the value for the fd-virus [51]. For simple shear flow, the relevant stress components are the shear stress (the viscosity), and the first and second normal stress differences. In terms of the

components of \mathbf{S} and $\mathbf{S}^{(4)}$, these are

$$\frac{\eta_p}{\eta_s \phi} = \frac{\sigma_{12,p}}{\eta_s \phi \dot{\gamma}} = \frac{\eta - \eta_s}{\eta_s \phi} = 2 \left(A S_{1122}^{(4)} + \frac{D_{r,0} F}{\dot{\gamma}} S_{12} \right), \quad (6)$$

$$\frac{N_1}{\eta_s \phi} = \frac{\sigma_{11,p} - \sigma_{22,p}}{\eta_s \phi} = 2(A \dot{\gamma} (S_{1112}^{(4)} - S_{1222}^{(4)}) + D_{r,0} F (S_{11} - S_{22})), \quad (7)$$

$$\frac{N_2}{\eta_s \phi} = \frac{\sigma_{22,p} - \sigma_{33,p}}{\eta_s \phi} = 2(A \dot{\gamma} (S_{1222}^{(4)} - S_{1233}^{(4)}) + D_{r,0} F (S_{22} - S_{33})). \quad (8)$$

The normalization of these quantities was chosen such that they are independent of particle concentration and solvent viscosity.

The dilute theory is applicable when the mean spacing between particles is large compared to their length, i.e., when $\phi \ll 4R^2/L^2$. Clearly, neither of the fd-virus dispersions considered in this work is close to satisfying this conditions. Beyond the dilute limit, there is no exact theory, although there have been a number of empirical extensions of the dilute theory to consider the semidilute regime [38,39,55,56]. Among these, one that has received recent attention, partly due to recent comparisons with data from fd-virus dispersions, is that due to Dhont and Briels with extensions by Lang *et al.* that we will refer to as the modified D-B model [39,40,47,57]. This theory is adapted in a recent paper, and we follow their presentation [40]. The key elements of the theory for the present study are again in Ref. [15].

III. THEORY FOR SAS AND DATA ANALYSIS VIA BAYESIAN ESTIMATION

In general, the *a priori* description of anisotropic scattering by oriented microstructures from requires two components. The first is a form factor model that takes as an input a real-space description of the distribution of scattering length density (SLD), ρ , within a geometrically defined particle shape and orientation, which is then averaged against the OPDF. The second is the physical theory, described in the previous section, that describes how the OPDF evolves due to the details of an imposed orienting field. Alternatively, the former can be used in closed form by “fitting” either the single-particle form factor and/or the OPDF to experimentally measured small-angle scattering (SAS) data.

A. Scattering theory: calculating the orientation-dependent form factor scattering

SAS measures the intensity with which radiation (e.g., neutrons, light) is scattered from a material as a function of the scattering wavevector, $\mathbf{q} = 4\pi \sin(\Theta/2)/\lambda$, where Θ is the scattering angle (made by the vectors of incident and scattered radiation) and λ is the wavelength of the incident radiation. We emphasize that \mathbf{q} is a vector, and so the scattering in general will depend on the direction of \mathbf{q} relative to the local orientation of the material (Fig. 1). We assume single elastic scattering events from a homogeneous dispersion of particles with uniform scattering length density (SLD). Under

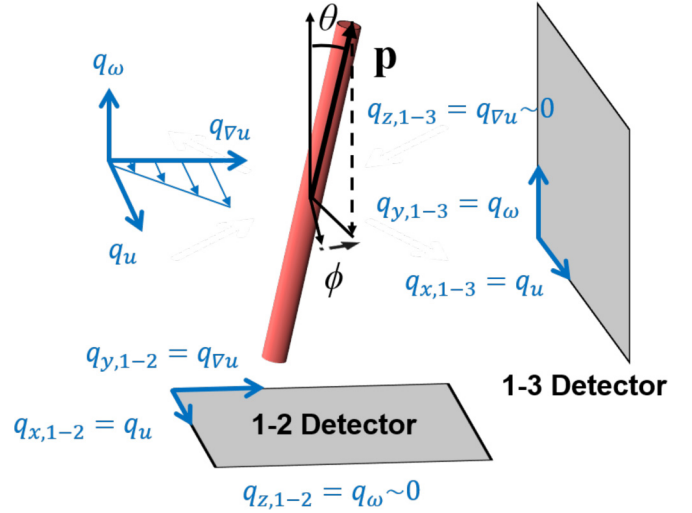


FIG. 1. The orientational coordinate system for a rod relative to the simple shear flow field indicated on the coordinate axis. The angles (ϕ, θ) provide information about particle orientation in the flow (q_u), gradient (q_{vu}), and vorticity (q_ω) directions. For the 1–2 and 1–3 sample environments, the relationship between the flow field and beam coordinate systems for the two sample environments used experimentally in this work are provided. In a real experiment, the direction of incident radiation (q_z) will not change, only the orientation of the flow relative to the incident radiation using different flow cells. Not pictured is the detector for the 2–3 plane, where incident radiation is along the flow direction.

conditions where intraparticle and interparticle scattering correlations do not interfere, the intensity of radiation scattered from a material at some \mathbf{q} , $I(\mathbf{q})$, is related to contributions from intraparticle scattering [the form factor, $P(\mathbf{q})$] and interparticle scattering [the structure factor, $S(\mathbf{q})$]

$$\overline{I(\mathbf{q})} = \Phi(\Delta\rho)^2 V_p \overline{P(\mathbf{q})S(\mathbf{q})} + b, \quad (9)$$

where Φ is the volume fraction of particles, $\Delta\rho$ is the SLD contrast between the particle and the suspending fluid, V_p is the average particle volume, and b is the incoherent scattering cross-section. The overbars in the expression signify ensemble averages of the quantities where, importantly, the product of the form factor and structure factor is the quantity being averaged on the right-hand side. For the experiments to which we will be comparing this framework, the measurements were made at low particle concentrations and in a sufficiently high \mathbf{q} -range where interparticle scattering effects are insignificant [i.e., $\overline{P(\mathbf{q})S(\mathbf{q})} \approx \overline{P(\mathbf{q})}$ for all measured \mathbf{q}]. Notably in SANS, one can measure or predict Φ , $\Delta\rho$ and the shape of the particle from other independent measurements.

The orientation of a 3D particle with arbitrary shape is uniquely defined by three orthogonal orientation vectors \mathbf{p}_1 , \mathbf{p}_2 , and \mathbf{p}_3 . If one only considers effects from orientation on the form factor, the measured form factor of such a particle is the macroscopic average of the single-particle form factor at all orientations weighted by the OPDF [1,28]. One can calculate this average form factor as

$$\overline{P(\mathbf{q})} = \iiint N(\mathbf{p}_1, \mathbf{p}_2, \mathbf{p}_3) P(\mathbf{p}_1, \mathbf{p}_2, \mathbf{p}_3; \mathbf{q}) d\mathbf{p}_1 d\mathbf{p}_2 d\mathbf{p}_3, \quad (10)$$

where $P(\mathbf{p}_1, \mathbf{p}_2, \mathbf{p}_3; \mathbf{q})$ is the form factor for a single particle at a single orientation and $N(\mathbf{p}_1, \mathbf{p}_2, \mathbf{p}_3)$ is the OPDF. The calculation of $P(\mathbf{p}_1, \mathbf{p}_2, \mathbf{p}_3; \mathbf{q})$ at a single, arbitrary orientation in 3D space is described in Ref. [15], with examples provided for cylindrical, parallelepiped, and ellipsoidal particles in Cartesian \mathbf{q} space. Equation (10) is completely general in that it makes no assumptions about the mathematical form of the OPDF or particle shape. In conjunction with recent advances in calculating form factors for particles at arbitrary orientations [58], this expands the range of microstructures and forms of OPDFs for which one may predict SAS patterns to monodisperse systems of arbitrarily shaped rigid particles with a known OPDF, that are sufficiently dilute (although not hydrodynamically dilute as required by the dynamical theory) such that $P(\mathbf{q})S(\mathbf{q}) = \overline{P(\mathbf{q})}$ in the \mathbf{q} -range considered. We will demonstrate later that both fd-virus dispersions considered in this work satisfy this criterion.

For this work, due to the axisymmetric shape of the fd-virus, the orientation of the particle is best described by one orientation vector, \mathbf{p} , in spherical polar coordinates (ϕ, θ) relative to a Cartesian simple shear flow field (Fig. 1) with q_u , $q_{\nabla u}$, and q_ω as the wavevector components in the flow (\mathbf{u}), gradient ($\nabla \mathbf{u}$) and vorticity ($\boldsymbol{\omega} = \nabla \times \mathbf{u}$) directions, respectively. We emphasize that θ defined here is not the same as Θ from the definition of \mathbf{q} . In what follows, we will sometimes refer to the flow, gradient and vorticity directions as 1, 2, and 3, respectively. In SAS measurements, scattering intensity is measured on a planar detector positioned very far from the sample relative to the detector size. As a result, measurements are typically assumed to be made in the $q_z \sim 0$ plane where z is the direction of incident radiation. Depending on the sample environment used, one may probe the structure in the $q_{\nabla u} \sim 0$ (flow-vorticity) plane for the 1–3 rheo-SANS sample environment or in the $q_\omega \sim 0$ (flow-gradient) plane for the 1–2 shear cell sample environment [20,21]. One can also configure the rheo-SANS sample environment such that measurements are made in the $q_u \sim 0$ (gradient-vorticity) plane; however, in this work, SAS was not measured in this plane due to complications from the curvature of the sample environment.

Equations (9) and (10) provide the general framework for computing the SAS from dilute, rigid particle dispersions. This framework can be utilized in two distinct ways: (1) in the “forward problem,” the physical theory for dilute, rigid particles in flow can be used to *predict* the OPDF and, therefore, the SAS intensity; and (2) in the “inverse problem,” the measured SAS intensity can be used to *infer* the OPDF. The use of the framework in these ways is predicated on one’s ability to derive orientation-dependent form factors for the particle, $P(\mathbf{p}; \mathbf{q})$, which must be validated for the system of interest. In this work, we validate a cylinder form factor to describe the fd-viruses by comparing equilibrium SAS measurements to SAS predictions with a uniform OPDF.

B. Model-free Bayesian inference method for inverting scattering integral equations

When the fluid is not dilute, hydrodynamic and direct interactions render the flow-induced particle dynamics too difficult

to solve, so that a rigorous Smoluchowski equation, equivalent to Eq. (1), cannot be formulated without simplifying assumptions such as those inherent in the derivation of the modified D-B model described previously. In this case, the only way to assess such a model is to develop a generalized framework for inferring OPDFs directly from experimental SAS data. Such an “inverse problem” is commonly encountered in scattering measurements, for which model-free solution approaches are highly sought due to their general applicability. Examples of such approaches are the use of constrained regularization algorithms for the parameter-free estimation of real-space density correlation functions from static scattering data [59], the structures of 2D lattices [60], or distributions of Brownian diffusion coefficients from dynamic scattering experiments [61].

In this work, we introduce a novel approach we call maximum *a posteriori* scattering inference (MAPSI) based on Bayesian estimation to solve for the OPDF from SAS measurements and a prescribed scattering model for the orientable particle. The general problem statement is to solve Eqs. (9) and (10) for $N(\mathbf{p})$, given the measured scattering intensity, $\overline{I(\mathbf{q})}$, and an expression for the single particle form factor as a function of \mathbf{p} and \mathbf{q} , i.e., $\Phi(\Delta\rho)^2 V_p P(\mathbf{q}, \mathbf{p})$. This problem represents a Fredholm integral equation of the first kind and is, therefore, fundamentally *ill-posed* (i.e., a solution does not exist that is stable against perturbations in the data). Regularization has been demonstrated as an effective method for numerically solving such problems, [62] but these methods have not been applied toward the inference of OPDFs from SAS. Recently, a Bayesian method was proposed to solve a similar *ill-posed* problem with the application of inferring nanoparticle size distributions from single particle tracking experiments [63]. Here, we adapt a similar mathematical framework for analysis of anisotropic scattering. We will briefly outline the method as it applies to extracting OPDFs from SAS experiments while a more rigorous description of the method is included in Ref. [15]. We note that MAPSI as outlined here is valid for axisymmetric particles but can be extended to include nonaxisymmetric particles by utilizing three angles to describe the orientation. Furthermore, our formulation of MAPSI applies no physical constraints on the OPDF and is therefore general to any particle and orienting field (e.g., biaxial simple shear flows), although additional constraints due to symmetry of the OPDF could be incorporated if desired. We will not incorporate such constraints in this work due to the known biaxiality of the OPDFs for particles in simple shear flow.

First, the unknown OPDF is discretized into a linear combination of hat functions in orientation space as $N(\mathbf{p}) = \sum_{m=1}^M w_m \chi_m(\mathbf{p})$, where M is the number of hat functions used to discretize the OPDF, $\chi_m(\mathbf{p})$ is a 2D spherical triangular hat function (see Ref. [15]) centered at a grid point indexed by m and is a function of orientation on the surface of the unit sphere S^2 , and w_m is the weighting for the hat function. Specifically, hat functions were generated on the 2-sphere by taking the convex hull of a sufficiently resolved Kurihara grid [64]. With this discretization, defining $\mathbf{p}_1 = \mathbf{p}$ as the only applicable orientation vector, and setting $\overline{P(\mathbf{q})S(\mathbf{q})} = \overline{P(\mathbf{q})}$,

Eqs. (9) and (10) become

$$\Phi(\Delta\rho)^2 V_p \int P(\mathbf{q}_k, \mathbf{p}) N(\mathbf{p}) d\mathbf{p} = \sum_{m=1}^M A_{k,m} w_m,$$

$$A_{k,m} = \Phi(\Delta\rho)^2 V_p \int P(\mathbf{q}_k, \mathbf{p}) \chi_m(\mathbf{p}) d\mathbf{p}. \quad (11)$$

The OPDF is restricted to satisfy the conditions $\int N(\mathbf{p}) d\mathbf{p} = 1$, $N(\mathbf{p}) \geq 0$ for all \mathbf{p} . These requirements yield the constrained optimization problem

$$\hat{\mathbf{w}}_m = \arg \max_{\mathbf{w}_m} \frac{-1}{2K} \sum_{k=1}^K \frac{1}{\sigma_k^2} \left[I(\mathbf{q}_k) - b - \sum_{m=1}^M A_{k,m} w_m \right]^2 + \lambda g(\mathbf{w})$$

s.t. $\mathbf{w} \geq 0$

$$\sum_{m=1}^M w_m = 1, \quad (12)$$

where K is the number of collected points in \mathbf{q} space, σ_k is the standard deviation of intensity of the k th wavevector (a known experimental quantity), and $\lambda g(\mathbf{w})$ is the log-prior, or regularization term. The regularization term is crucial for addressing the *ill-posedness* of the underlying problem and ensuring that the scattering intensity does not overfit the data and produce artificially sharp peaks in the OPDF [59,63]. In this case, we define the regularization term as the integral of the square of the gradient of the OPDF, which can be represented as a quadratic form in the weights and results in an optimization problem that can be efficiently solved with a quadratic programming solver. The hyperparameter, λ , which governs the strength of the regularization term, is found *via* cross validation in order to prevent overfitting when dealing with a finite amount of data. See Refs. [15,63] for additional details on the cross-validation procedure.

The function $\chi(\mathbf{p}_m)$ was chosen as the means of discretizing the OPDF to simplify the numerical scheme by enabling one to cast the optimization as a quadratic problem and allowing for one to easily constrain $N(\mathbf{p}) \geq 0$ for all \mathbf{p} . In Ref. [15], we demonstrate that hat functions can approximate smooth functions on the surface of a sphere to arbitrary accuracy.

We specifically emphasize for studies that utilize different detector planes that one may specify the measured wavevectors (\mathbf{q}_k 's) that are included for extracting the OPDF. For example, in this work we will consider extracted OPDFs that utilize measured wavevectors from a single measurement plane (i.e., using measurements from only the 1–2 or 1–3 sample environment) or from two measurement planes (i.e., using measurements from both the 1–2 and 1–3 sample environments). This will allow us to assess the information that is gained or lost from measurements in a particular plane. For data sets that combine measurements from different planes, it is crucial that \mathbf{q} vectors are expressed with respect to the same reference frame (in this case the flow field, see Fig. 1).

MAPSI presents distinct advantages over other methodologies that determine OPDFs from SAS measurements. Compared to more conventional fitting strategies, this method makes no assumptions about the mathematical form of the OPDF. We note that the recently proposed spherical harmon-

ics expansion shares this advantage [14]. Unique to MAPSI is the use of and search for the regularization parameter λ . Addressing the *ill-posedness* of the inference problem requires the use of a regularization term to avoid overfitting. Rather than arbitrarily choosing the strength of the regularization term, λ , MAPSI utilizes cross validation to find a value of λ that is most consistent with the data under measurement uncertainty. SAS measurements have inherent uncertainty given the spread in incident neutron wavelength and finite measurement time of experiments, which should be reflected in any parameter extracted from the measurement. Given the Bayesian nature of MAPSI and more specifically the search for λ (via cross validation), these uncertainties are naturally propagated through the analysis to the posterior distribution of the weights, which we sample with a Monte Carlo scheme in order to extract measures of error for derived quantities of the distribution. In this work, we will use such a sampling procedure to extract moments of the OPDF with error bars that represent the standard deviation of the full posterior probability distribution of moments or other derived quantities.

IV. RESULTS AND DISCUSSION

A. Near-equilibrium 1D scattering for validation of scattering model

To validate the single-particle scattering model (i.e., $\Phi(\Delta\rho)^2 V_p P(\mathbf{q}, \mathbf{p})$) used to describe the SAS from the fd-virus dispersion, we compare the isotropic predictions of the scattering model for the fd-virus with equilibrium SANS measurements. As mentioned before, the fd-virus used in this work is typically modeled as a cylinder with radius, $R = 3.3$ nm, and length, $L = 920$ nm [46,47]. The fd-virus scattering length density (SLD) was calculated to be $\rho_{\text{SLD},p} = 3.03 \times 10^{-6} \text{ \AA}^{-2}$ using the “Biomolecular SLD Calculator” available through ISIS and the known protein sequence for the virus [65]. The solvent SLD was fixed at that of pure D_2O ($\rho_{\text{SLD},s} = 6.33 \times 10^{-6} \text{ \AA}^{-2}$, although one may expect the solvent D_2O to be slightly lower due to the added buffer. The incoherent background scattering was calculated from a linear fit of a plot of q^4 versus Iq^4 , where the slope of the line is equal to the background. The only remaining parameter, the concentration of the fd-virus, is determined from a fit of the measured equilibrium scattering. We stress that the only adjustable parameter in the fit is one relating to the absolute magnitude of the scattering signal, and so the shape of the scattering curve is fixed from the known particle shape. The fits and subsequent analyses were made in the q range from 0.02 to 0.2 \AA^{-1} .

The equilibrium structure at zero shear rate was probed for the two different concentration dispersions and in the two detector planes. These equilibrium measurements, corrected for the incoherent scattering cross section (I_{incoh}), which is extracted from the measurement, and normalized by the volume fraction, are included in Fig. 2. Also included is a prediction of the scattering intensity for the fd-virus, modeled as a cylindrical particle with the dimensions mentioned previously. We find that the normalized equilibrium scattering from the samples in both the 1–2 and 1–3 planes are well described by this scattering model, with no included structure factor, validating

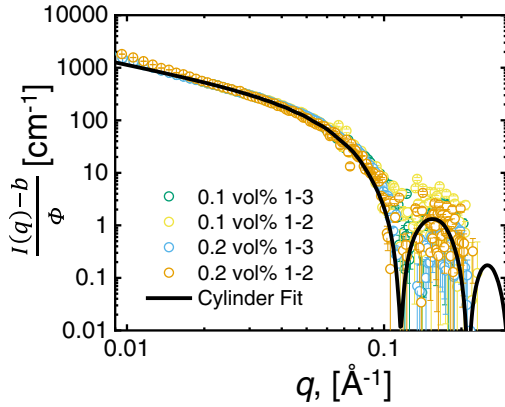


FIG. 2. 1D equilibrium SANS measurements and fits for the fd-virus dispersions considered in this work. The measured intensities are corrected for incoherent scattering and volume fraction extracted from fits of the measurements. Measurements are included for the concentrations (0.1 and 0.2 vol%) and measurement planes (1–2 and 1–3) as the open points of varying color where the error bars indicate the standard deviation of the intensity from the SANS measurement. The cylinder model considered for the fd-virus is included as the black line.

its use in the following sections for all concentrations and detector planes.

B. Parameter-free extraction of the 3D OPDF using MAPSI: method validation

In the theory section, we described a method, MAPSI, that can be used for determining OPDFs from experimental measurements. To validate the method, we conduct numerical simulations using the dilute particle theory to *predict* SAS

patterns in the 1–2, 1–3, and 2–3 measurement planes, which are then used as an input to MAPSI. Utilizing predictions from dilute theory with no added noise enables us to assess the utility of MAPSI for accurately extracting OPDFs free from the influence of nonidealities in the experimental system or uncertainties in the measured scattering intensity. Any deviation of the extracted OPDF from the OPDF used to generate the scattering therefore represents errors introduced from either the limited \mathbf{q} -resolution in the predicted scattering patterns or from MAPSI itself.

Numerical simulations of the OPDF for dilute rodlike particles matching the dimensions of the fd-virus in simple shear flow were carried out as a function of rotational Péclet number, Pe_r . The OPDFs were used with the validated fd-virus scattering model to generate SAS predictions in the 1–3, 1–2, and 2–3 measurement planes with the same \mathbf{q} range and \mathbf{q} resolution measured in experiments. The predicted SAS patterns were then used as input to MAPSI to extract OPDFs. Since MAPSI requires information about measurement errors, the standard deviation of the intensity was set to $0.33I(\mathbf{q})$, representative of the value of the standard deviation in the SAS measurements. A smaller value was found to have no observable effect on the inferred OPDFs.

Representative OPDFs for $Pe_r = 2, 7.5$, and 30 are included in Fig. 3, including the OPDF predicted from theory and extracted from MAPSI using scattering from the 1–3 plane, 1–2 plane, both the 1–2 and 1–3 planes, and all three planes. For all extracted OPDFs, as Pe_r is increased, the apparent OPDF becomes increasingly peaked. Importantly, when comparing the OPDF extracted from all three scattering planes simultaneously, we find that the full OPDF is nearly quantitatively recovered, validating the MAPSI method. By contrast, when an incomplete set of scattering projections is used, the apparent most likely orientation [corresponding

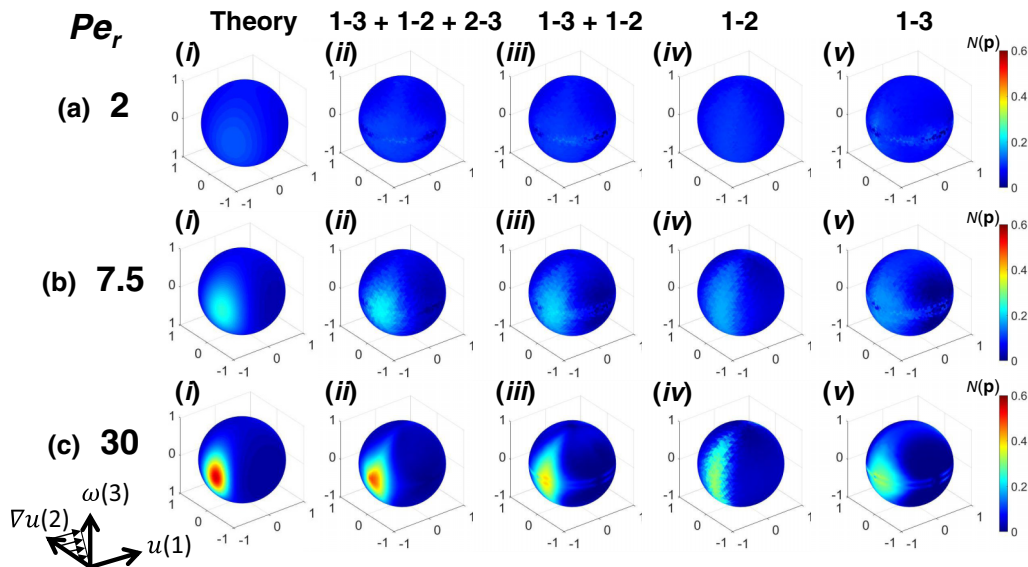


FIG. 3. Representative 3D OPDFs (i) simulated from dilute theory and extracted from MAPSI using theory-predicted scattering in the (ii) 1–2, 1–3, and 2–3 planes, (iii) 1–2 and 1–3 planes, (iv) 1–2 plane and (v) 1–3 plane. For the 1–3 scattering, the incident radiation is in the ∇u (2) direction; for the 1–2 scattering, the incident radiation is in the ω (3) direction; and for the 2–3 scattering, the incident radiation is in the u (1) direction. The representative results are included for $Pe_r =$ (a) 2, (b) 7.5, and (c) 30. The color on the unit sphere represents the value of the OPDF in a particular direction in the u , ∇u , and ω reference frame specified in the bottom left corner. The black lines on the unit sphere indicate the edges of the hat functions used to discretize the OPDF.

to the peak in $N(\mathbf{p})$ depends on the measurement planes utilized. For 1–3 plane measurements, the most likely orientation coincides with the flow direction, about which the OPDF is symmetric, whereas for 1–2 plane measurements it lies slightly away from the flow direction toward the gradient direction, which is expected from the dilute theory. Additionally, the OPDF extracted from the 1–2 plane scattering is broadened along the vorticity direction compared to that extracted from 1–3 plane scattering. For the extractions combining measurements (1–3 + 1–2 and 1–3 + 1–2 + 2–3), the axis of symmetry of the OPDF is tilted into the gradient direction similar to the 1–2 plane, yet is more weakly broadened in the vorticity direction than for the former case. When comparing the OPDF extracted from the 1–2 and 1–3 scattering to the theory-predicted OPDF, we find that the peak location in $N(\mathbf{p})$ is accurately captured, while its value is underestimated, which we attribute to the spreading of probability in the vorticity direction compared to the underlying OPDF. For several of the OPDFs we also note the presence of “ridges,” most significantly along $\omega = 0$. We attribute the presence and locations of these ridges to regions of the OPDF where the included SANS measurements provide little information. In other words, these regions correspond to areas where the particle is perfectly aligned or just off alignment from the plane of measurement. Since we are not probing a \mathbf{q} -range corresponding to the full length of the particle, it can be expected that such regions would exist in the OPDF. We do not observe such ridges in the OPDFs determined from experimental measurements, and therefore attribute the absence of ridges to the regularizing effect of measurement uncertainty.

We now summarize the effects of utilizing scattering from different detector planes (i.e., projections of structure) on the extracted OPDF relative to that extracted using all three detector planes. For OPDFs extracted from the 1–3 plane only, the OPDF is broadened along the flow gradient direction, and the most probable orientation always lies exactly in the flow direction. For the OPDF extracted from the 1–2 plane scattering, the OPDF appears to be broadened along the vorticity direction, and the most probable orientation shifts from 45° between the flow-flow gradient directions at low shear rates to nearly the flow direction at high shear rates. Both results are due to the loss of out-of-plane orientational information when restricting analysis to a single scattering projection plane. We suggest that this occurs because the form factor when $q_z = 0$ (where z is the direction of incident radiation) is symmetric with respect to $\Theta = 0$, where Θ is the orientation of the particle out of the plane of measurement. Qualitatively, one can understand this effect as analogous to projections in real-space measurements, where particle orientations in the $\pm\Theta$ direction cannot be distinguished. In the case of the 1–3 plane scattering, $\Theta = \phi$ and $q_z = q_{\nabla u}$, which leads to the measured symmetry about the flow direction in the extracted OPDF because one cannot distinguish between orientations in the $\pm\phi$ direction. Finally, OPDFs extracted from 1–3 + 1–2 scattering planes appears to have artificially smoothed features, but do not qualitatively differ from the case where all three planes are used. We conclude that accurately resolving the full OPDF from SAS requires measurement and analysis of at least two different detector planes.

The preceding analysis *qualitatively* demonstrates the loss of information regarding the 3D OPDF generally incurred by an analysis of anisotropic scattering when analysis is restricted to a single scattering plane. A more *quantitative* analysis of this information loss can be assessed by examining various scalar moments of the OPDF. Given that MAPSI accurately resolves the full OPDF, one could theoretically calculate moments of the OPDF (and propagated errors of such moments) to arbitrarily high order. Here, we restrict the analysis to include only the second and fourth moments of the distribution, \mathbf{S} and $\mathbf{S}^{(4)}$. As mentioned previously, these moments are required to determine various material properties, such as the particle contribution to the mechanical stress in force-free orientable particle systems [12].

The results for the nonzero components of the second moments, \mathbf{S} , are included in Fig. 4. We show results including scattering measurements in single detector planes (the 1–2 and 1–3 planes), in both the 1–2 and 1–3 planes, and in three orthogonal planes (1–2 + 1–3 + 2–3) for q in the range from 0.02 to 0.2 Å, which corresponds to that available in the experiments. We see that the agreement for the diagonal components of \mathbf{S} obtained via MAPSI and the exact results is excellent in cases where multiple projection planes are used. The only modest disagreement is for S_{12} , where the peak values obtained via MAPSI are smaller and there appears to be a slight shift toward smaller values of Pe_r , both for the two-plane and three-plane cases. The three-plane result is clearly better than the two-plane result, though both cases show errors of similar magnitude. The main reason why the 3-plane result still shows a difference from the exact result for S_{12} is that the data are restricted to a limited q -range for this comparison, in an attempt to capture experimental conditions. Of course, for the dilute suspension case that we are considering in this section, we can calculate the scattering patterns for arbitrary q , and then explore how the results from MAPSI would change if we had data for a wider range of q . One example where the q range is extended to include 0.002 to 0.2 Å is included in Fig. 4. The agreement between the MAPSI extracted moments and the dilute theory clearly demonstrates that a very accurate result could be achieved if data were available over a wider range of q . The components of \mathbf{S} define a first approximation of the shape of the OPDF in the form of an ellipsoid. At equilibrium, the shape is a sphere (the diagonal components are nonzero and equal while the off-diagonal components are zero). The first departure is a distortion in the principle straight direction ($S_{12} > 0$), followed by elongation of the ellipsoid and rotation toward the flow axis. The fact that the peak in S_{12} is underestimated means that the OPDF obtained via MAPSI shows somewhat less alignment and distortion in the direction of the principle strain-rate axis than actually occurs. According to Eq. (6), this would produce an underestimate of the shear viscosity at Pe_r of $O(10)$ if we used the OPDF obtained via MAPSI.

Due to tensor symmetries and the symmetry of the shear flow field, there exist nine unique, nonzero scalar components for the fourth-order tensor, $\mathbf{S}^{(4)}$ (Fig. 3). While other studies have resolved the diagonal components of the second moment tensor with measurements in multiple detector planes [47], to our knowledge, the current work represents the first means of measuring the off-diagonal terms for nonspherical

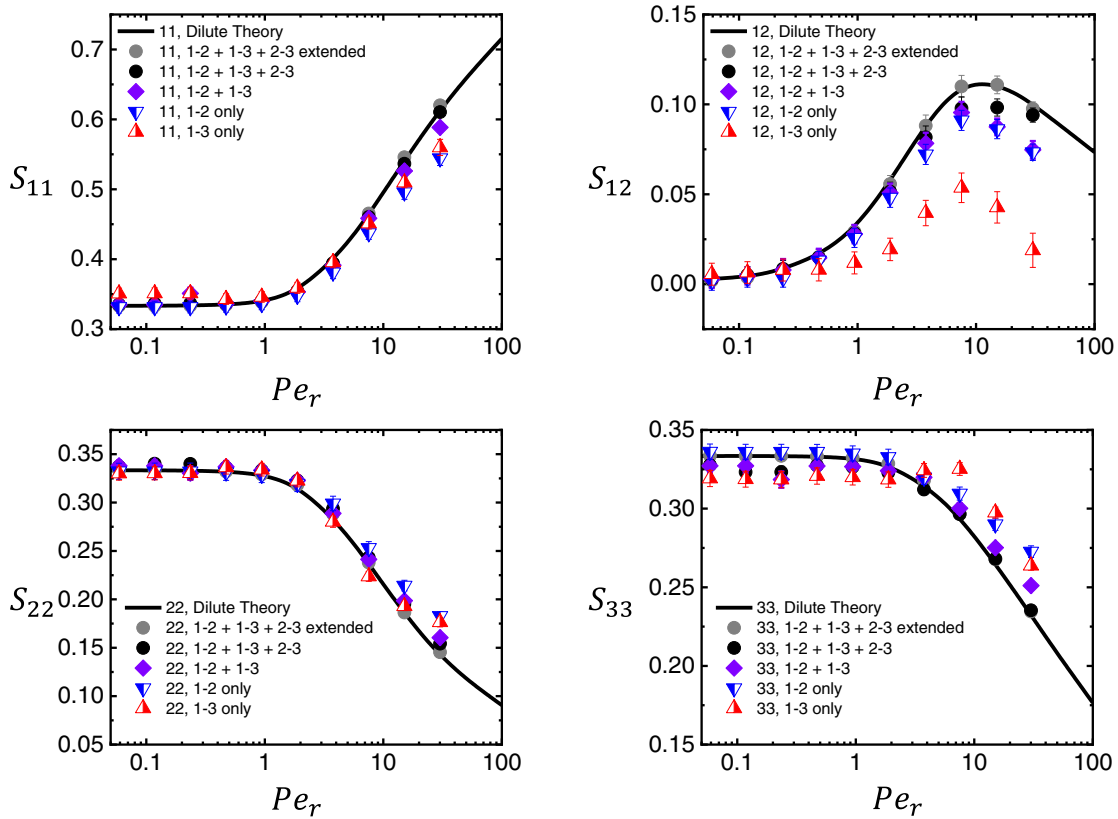


FIG. 4. Components of the second moment tensor, \mathbf{S} , calculated from simulations of the dilute rod theory (black lines) and calculated from OPDFs extracted from MAPSI using theory predicted scattering (points) at varying Pe_r . Components of the moment tensor extracted using MAPSI include results using data from different scattering projections included: 1–2 plane only (up-pointing red triangles with right side filled), 1–3 plane only (down-pointing blue triangles with left side filled), using both 1–2 and 1–3 plane scattering (purple filled diamonds), using 1–2 + 1–3 + 2–3 plane scattering (filled black circles) and using 1–2 + 1–3 + 2–3 plane scattering with an extended q -range (filled gray circles). The error bars indicate the standard deviation of the value from posterior sampling where the standard deviation was taken to be $I(\mathbf{q})/3$.

nanoparticles simultaneously utilizing multiple SAS projections, and therefore this necessitates a discussion of the information about $\mathbf{S}^{(4)}$ that is lost or gained from scattering information in a particular plane. In order to facilitate this discussion, the moments have been divided into the three diagonal components $S_{1111}^{(4)}$, $S_{2222}^{(4)}$, and $S_{3333}^{(4)}$, the three symmetric off-diagonal components $S_{1122}^{(4)}$, $S_{1133}^{(4)}$, and $S_{2233}^{(4)}$, and the three antisymmetric components $S_{1112}^{(4)}$, $S_{1122}^{(4)}$, and $S_{1233}^{(4)}$.

For the diagonal components, $S_{1111}^{(4)}$ increases whereas $S_{2222}^{(4)}$ and $S_{3333}^{(4)}$ decrease with increasing shear rate, regardless of the data used in MAPSI (Fig. 5, first row). In the case of both $S_{1111}^{(4)}$ and $S_{3333}^{(4)}$, we find that only including the scattering data in the 1–3 or 1–2 measurement plane leads to a quantitative underestimate compared to simultaneously using data from both of these planes, which is more severe for measurements in the 1–3 plane. For $S_{2222}^{(4)}$, including only information from the 1–3 plane yields a value that is quantitatively similar to the result when both planes are included, while only including the 1–2 plane measurement overpredicts $S_{2222}^{(4)}$. For the diagonal components, including multiple planes in the analysis significantly reduces these errors (with absolute errors less

than 0.04 and 0.008 when using the 1–2 and 1–3 planes or the 1–2, 1–3 and 2–3 planes, respectively).

For the symmetric off-diagonal components of the moment tensor (Fig. 5, second row), we find an increase followed by a decrease in the values $S_{1122}^{(4)}$ and $S_{1133}^{(4)}$, while we find a monotonic decrease in the value of $S_{2233}^{(4)}$ with increasing shear rate. For $S_{1122}^{(4)}$, we find that only including the information from the 1–2 measurement leads to a slight underestimation of the value, while only including 1–3 measurement information overestimates the value of the component compared to utilizing all the measured intensities. For $S_{1133}^{(4)}$, using only 1–3 plane information correctly infers the values while using only 1–2 plane information leads to an overestimate. For $S_{2233}^{(4)}$, using only the 1–2 plane measurement tends to slightly overestimate the value while using only the 1–3 plane correctly infers the value. Again, including information from two or more planes leads to very small errors between the “true” values and those estimated by MAPSI.

For the antisymmetric components of the moment tensor (Fig. 5, third row), the $S_{1112}^{(4)}$, $S_{1122}^{(4)}$, and $S_{1233}^{(4)}$ component values increase and then decrease with increasing shear rate.

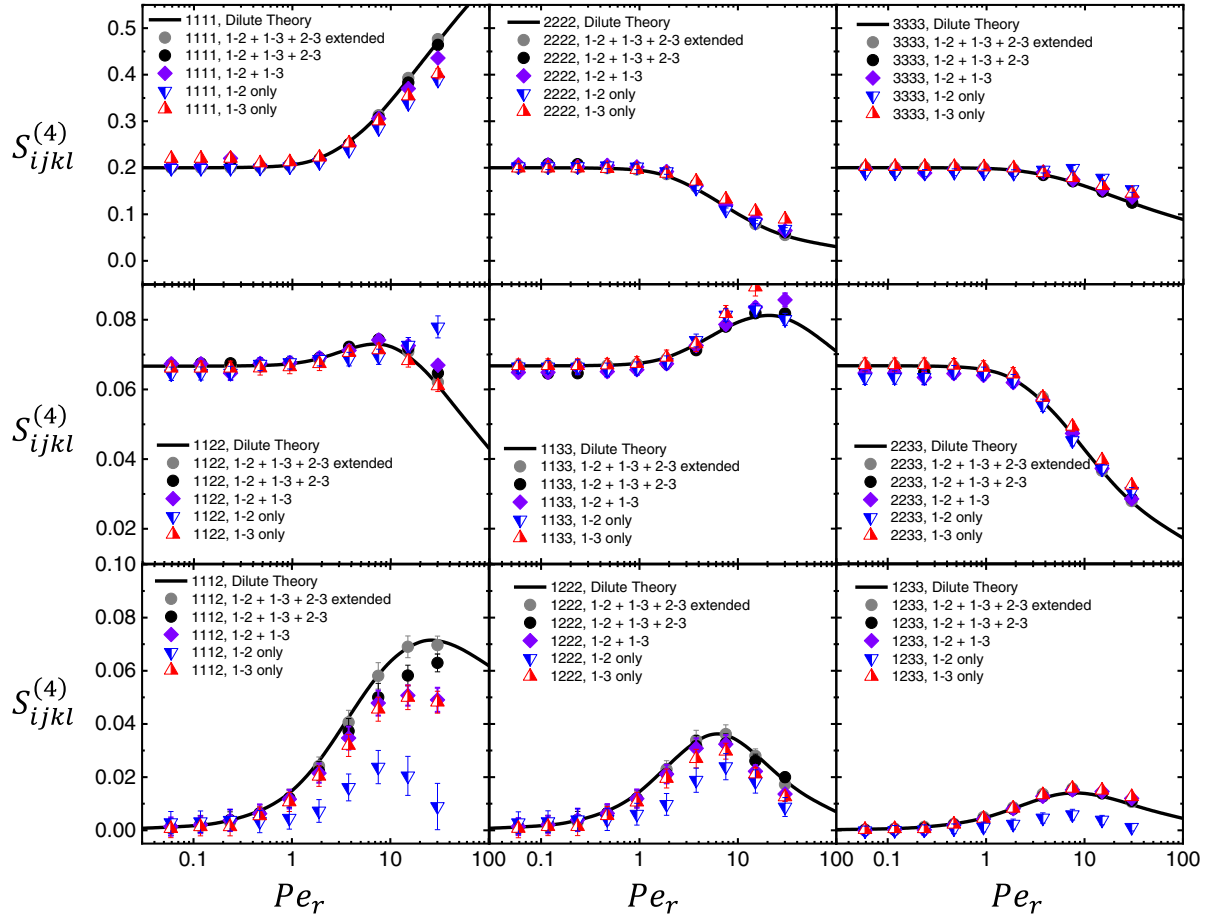


FIG. 5. Components of the fourth moment tensor, $S^{(4)}$, calculated from simulations of the dilute rod theory (black lines) and calculated from OPDFs extracted from MAPSI using theory predicted scattering (points) at varying Pe_r . The component of the moment tensor is indicated in the legend, where the four numbers correspond to the i, j, k and l indices for the moment. Components of the moment tensor extracted using MAPSI include results using data from different scattering projections included: 1–2 plane only (up-pointing red triangles with right side filled), 1–3 plane only (down-pointing blue triangles with left side filled), using both 1–2 and 1–3 plane scattering (purple filled diamonds), using 1–2 + 1–3 + 2–3 plane scattering (filled black circles) and using 1–2 + 1–3 + 2–3 plane scattering with an extended q -range (filled gray circles). The error bars indicate the standard deviation of the value from posterior sampling where the standard deviation was taken to be $I(\mathbf{q})/3$.

For all of these components, only utilizing the information from the 1–3 measurement leads to a severe underestimate for these components, and only utilizing the information from the 1–2 measurement leads to a similar value of the components as when both 1–2 and 1–3 plane measurements are used. Again, in most cases using two or more planes significantly improves the accuracy of estimates from MAPSI. However, this is not true for $S_{1112}^{(4)}$, even when including measurements in the 1–2, 1–3, and 2–3 planes. However, when a wider q range is included, MAPSI correctly predicts the value of $S_{1112}^{(4)}$ and all components of the fourth moment tensor.

Overall, we find excellent quantitative agreement between fourth moments determined from the known exact OPDF and those obtained using MAPSI when two or three measurement planes are used. As commented on previously, a general feature of the OPDFs inferred from measurements in a single detector plane is a loss of information about the OPDF in

the out-of-plane direction. The clearest illustration of this from the moment analysis is the severe underprediction of values for the antisymmetric components from 1–3 plane measurements. These antisymmetric components describe the asymmetry of the OPDF around the velocity direction due to the biaxial nature of the shear flow. From the full OPDF [Fig. 3(c)], we can directly observe this loss of asymmetry. Furthermore, we have quantified the errors expected for particular moments, which will be used in the analysis of moments extracted from experimental data to follow. The results for the second and fourth moments make it clear that the accuracy in extracting moments improves further with a wider q range, but such extended q ranges were logistically unrealizable for the dilute dispersions considered in this work. Therefore, one must consider the potential errors arising from sampling a limited q range. For now, we consider these reported errors to be expected for each of the components

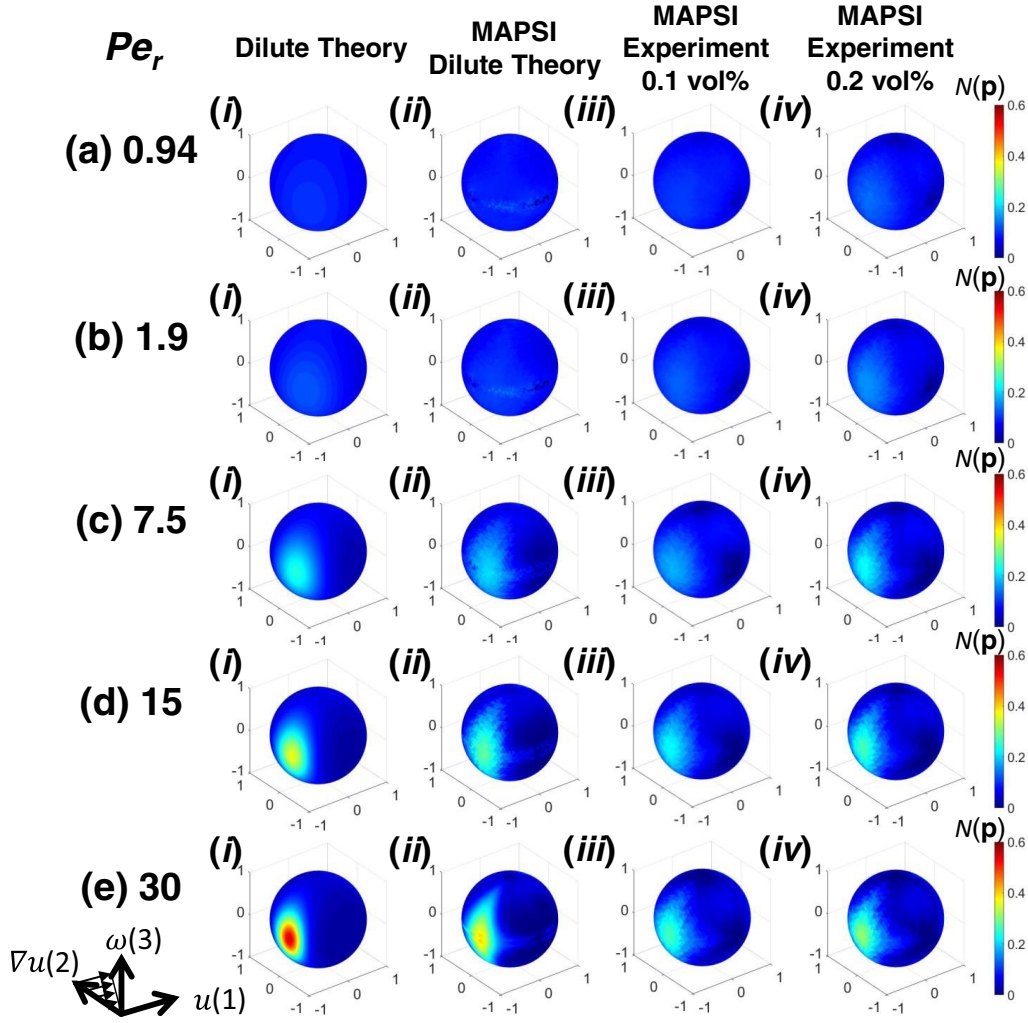


FIG. 6. A comparison of OPDFs from (i) dilute theory to those inferred by MAPSI using (ii) dilute theory predictions of SANS in the 1–3 and 1–2 planes and (iii, iv) experimentally measured SANS of the fd-virus dispersions at 0.1 and 0.2 vol%. For the 1–3 measurement, the incident radiation is in the $\nabla u(2)$ direction, while for the 1–2 measurement, the incident radiation is in the $\omega(3)$ direction. The representative results are included for Pe_r of (a) 0.94, (b) 1.9, (c) 7.5, (d) 15, (e) 30 ($\dot{\gamma} = 16, 32, 128, 256$, and 512 s^{-1} , respectively). The color on the unit sphere represents the value of the OPDF in a particular direction in the u , ∇u , and ω reference frame specified in the bottom left corner. The black lines on the unit sphere indicate the edges of the hat functions used to discretize the OPDF.

from utilizing MAPSI with the measured \mathbf{q} range relative to the characteristic size of the particle considered in this work.

C. Parameter-free extraction of the 3D OPDF for fd-virus dispersions at $\phi/\phi^* \cong 1$ and 2

We now utilize MAPSI to extract the 3D OPDF from experimental flow-SANS measurements under shear in the 1–2 and 1–3 planes of measurement for the two semidilute fd-virus dispersions. A comparison of SANS patterns measured for the more dilute dispersion and predicted from the dilute theory (Appendix A) shows that the SANS patterns are qualitatively different from those predicted from the dilute suspension theory (see Figs. 10 and 11). Using MAPSI will therefore enable us to directly quantify the aspects of the OPDFs inferred from experiments that deviate from the dilute theory. In the process, we explore the extent to which

particle interactions for semidilute fd-virus dispersions cause the OPDF to deviate from that for the dilute limit.

MAPSI was used to extract OPDFs from SANS measurements from $Pe_r = 0.06$ (where no anisotropy was observed in the measured patterns) to $Pe_r = 30$ (where significant anisotropy was observed). We therefore expect MAPSI to infer isotropic OPDFs for smaller shear rates and more anisotropic OPDFs with increasing shear rate. Figure 6(iii) includes representative results for the fd-virus dispersions. We also include the OPDF from the dilute theory [Fig. 6(i)] and the corresponding inferred OPDF using MAPSI and predictions of the scattering from the dilute theory in the 1–3 and 1–2 planes [Fig. 6(ii)]. Since the experimental measurements were only made in the 1–3 and 1–2 planes, the latter represents what we would expect to infer from measurements if the experimental system has the exact same structure as that predicted from the dilute theory. At low Pe_r and for all the OPDFs, we find that the resulting OPDF is nearly isotropic for all orientations, as expected for a dispersion at small Pe_r .

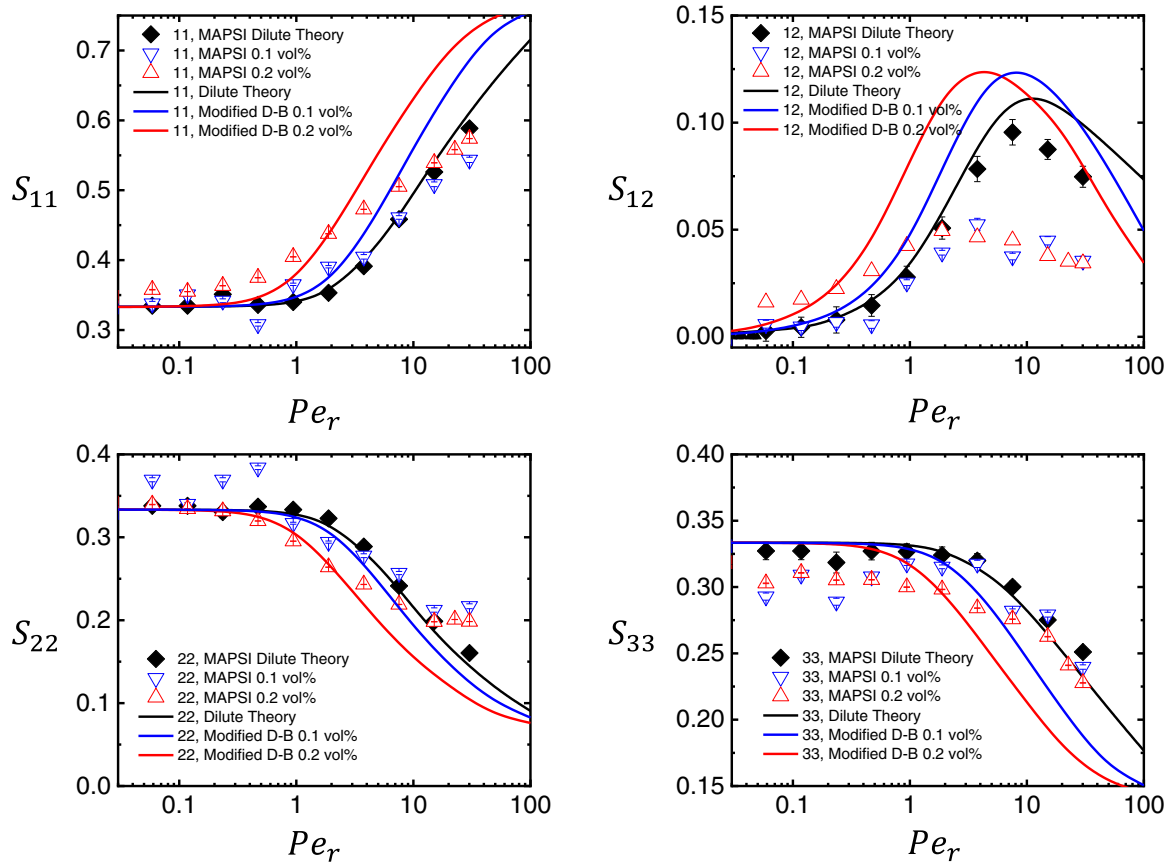


FIG. 7. Components of the second moment tensor, \mathbf{S} , calculated from simulations of the dilute rod theory (black lines), simulations of the modified D-B model (colored lines), and calculated from OPDFs extracted from MAPSI using experimentally measured scattering (colored points) at varying Pe_r . Concentrations of 0.1 vol% (blue) and 0.2 vol% (red) corresponding $\phi/\phi^* \approx 1$ and 2 are included. The solid black points are moments extracted from MAPSI and dilute theory predictions of the scattering in the 1–2 and 1–3 planes (Fig. 4). The error bars indicate the standard deviation of the value from posterior sampling.

As Pe_r is increased, the OPDFs become increasingly peaked. All three OPDFs show a similar direction of most probable alignment, which shifts from 45° between the flow and gradient directions to the flow direction with increasing Pe_r . As discussed in the previous section, the OPDFs inferred from MAPSI using only scattering in the 1–2 and 1–3 planes have maxima that are quantitatively smaller than the OPDF from the dilute theory, which is clearer at higher shear rates.

We will now compare the OPDFs inferred using MAPSI based upon the theoretically-predicted SANS patterns from the dilute theory and the experimentally measured SANS patterns for the fd-virus. When comparing the MAPSI inferred OPDFs from theory and experiment, we find that those inferred from experiments have a smaller maximum in the OPDF than those inferred from theory. This difference is not surprising, given the previous analysis of the differences in the scattering patterns that were used to infer the OPDFs (see Appendix, Figs. 10 and 11). Other than the differences in the maximum value of the peak, we find few qualitative differences between the two OPDFs, and the OPDFs display striking similarity overall. As previously mentioned, both OPDFs begin to show deviations from uniformity at similar Pe_r (near 1). For all Pe_r , both OPDFs have a similar shape to the peak in the OPDF (probability is stretched more along

the vorticity direction than the gradient direction, and this asymmetry increases with increasing Pe_r). Comparing the experimental OPDF to the theory OPDF [Figs. 6(ii) and 6(iii)], we note that probability is slightly more spread out in the $\omega = 0$ plane and slightly less spread out in the $\nabla u = 0$ plane in the experiment than in the theory. However, these differences are difficult to resolve at this level. To assess the differences between the OPDFs, we turn to an analysis of the moments of the OPDFs, which will provide a quantitative description of the differences in the structure between the dilute theory and the experimental measurements of the fd-virus dispersion.

Again, we begin with the second moment tensor, \mathbf{S} . The results for the two experimental fd-virus dispersions are included in Fig. 7, together with the exact results for the dilute suspension, and for the dilute suspension inferred by MAPSI from the calculated SAS patterns [see Appendix B] in similar planes of measurement (1–2 + 1–3). Starting with the diagonal components of \mathbf{S} (S_{11} , S_{22} , and S_{33}), we find that the lowest concentration fd-virus is similar to the results for the dilute suspension, but that there are significant differences for the more concentrated dispersion. In the latter case, the component in the flow direction (S_{11}) is larger between $Pe_r \approx 0.5$ and 20 and departs from the equilibrium value at a lower value of Pe_r , while the components in the gradient (S_{22})

and vorticity (S_{33}) directions are smaller in this Pe_r range. Recalling that the second moments are related to the shape of the OPDF, viewed as an ellipsoid, we see that the OPDF is more elongated and oriented toward the flow direction and flattened in the gradient and vorticity directions relative to the predicted shape for a dilute suspension. Interestingly, the values of the diagonal components are similar at high Pe_r for both experimentally measured dispersions. Larger differences between experiment and theory are observed in the S_{12} component, with the values very much reduced for Pe_r greater than $O(1)$. While the two dispersions are similar in this regime, the more concentrated dispersion deviates from both the dilute suspension and from the lower concentration dispersion at significantly lower Pe_r . Both this result and the earlier departure of S_{11} from its equilibrium value are indicative of the fact that the relaxation time of the fluid is significantly increased as a consequence of particle interactions.

An obvious question is whether the modified D-B model for semidilute suspensions provide a better fit to the experimental data. An indication of the answer is shown in Fig. 7 as a comparison between the experimental data, the dilute suspension results, and predictions from the modified D-B model for the components of \mathbf{S} . For the symmetric components of \mathbf{S} , we find that the modified D-B model captures the initial deviations from the dilute theory but fails to at high shear rates. In particular, we find that the diagonal components of \mathbf{S} have concentration-independent values at the largest measured shear rates ($Pe_r \approx 30$), while the modified D-B model predicts that concentration will have a significant effect at these shear rates. This result suggests that the modified D-B model overpredicts the impact of interparticle interactions when the particles are significantly aligned to an extent that cannot be explained solely by the effects of finite q -range sampling discussed previously. For the S_{12} component, the modified D-B model does not predict the lower value measured at high shear rates ($Pe_r > 2$). These deviations are larger than those resulting from only using measurements in the 1–3 and 1–2 detector planes, suggesting that measurement errors are not a sufficient explanation for the observed deviations. Therefore the way the modified D-B model accounts for interparticle interactions does not explain all the deviations between the measured and theoretical value of S_{12} , and new theoretical developments will be needed to explain this measured result. One possible area for improvement in the model is the expression for the diffusivity. In particular, the modified D-B model interpolates between small and high degrees of alignment, and it is possible that this interpolation underpredicts how quickly the diffusivity of the rods approaches the dilute limit with increasing particle alignment. These measurements could be used to provide more accurate interpolation between the near-equilibrium diffusivity provided with the Doi expression and the fully aligned diffusivity provided by the expression for dilute rods.

As discussed in the previous section, an important additional quantitative description of the OPDFs may be achieved through the calculation of the fourth moment tensor, $\mathbf{S}^{(4)}$. Figure 8 includes the components of the fourth moment tensor with error propagated from the SANS measurement. We also include the moments as predicted from the dilute theory

and moments extracted from the MAPSI inferred OPDFs using dilute theory predictions for the scattering. We do not include predictions from the modified D-B model, as the model utilizes a closure approximation and does not make predictions for the fourth moments of the OPDF. Detailed investigations of the applicability and accuracy of closure approximations in general will be the subject of future studies. Due to the information lost from only using measurements in the 1–2 plus 1–3 planes, the proper comparison between theory and experiment is between the respective MAPSI inferred moments.

For the diagonal and symmetric off-diagonal components of $\mathbf{S}^{(4)}$ over the whole range of Pe_r , we find good agreement overall between the moments derived from experiment and theory. We do observe fluctuations in the values of the experiment-derived moments at low shear rates, where the value is expected to be nearly constant. We attribute these fluctuating values to slight variations in the magnitude of the scattering intensity between measurements, which affects the single particle scattering model [i.e., $\Phi(\Delta\rho)^2 V_p P(\mathbf{q}, \mathbf{p})$] that describes the system. In reality, the particle scattering model validated at equilibrium will itself have errors, which should also be propagated into the derived moments and standard deviations of moments. Incorporating these types of uncertainties is beyond the scope of this work, and these magnitudes of variations do not affect the conclusions to follow.

The most notable deviations between the experiment and theory occur at $Pe_r > 1$, and this is particularly true for the antisymmetric components. We will focus on two aspects of the differences for only the 0.1 vol% dispersion, as the dispersion at this concentration is better described by the dilute theory than the 0.2 vol% dispersion. The two most notable deviations are for several of the components of $\mathbf{S}^{(4)}$ at $Pe_r = 30$ and deviations in the antisymmetric components ($S_{1112}^{(4)}$, $S_{1222}^{(4)}$, and $S_{1233}^{(4)}$) for all $Pe_r > 1$. At $Pe_r = 30$, the experiments yield a larger value of $S_{2222}^{(4)}$, $S_{1122}^{(4)}$, and $S_{2233}^{(4)}$ and a smaller value of $S_{1111}^{(4)}$, $S_{1133}^{(4)}$, and the antisymmetric components. As noted previously, the onset of a Taylor instability is expected to occur for a Newtonian fluid of similar viscosity and density as the fd-virus dispersion when $Pe_r \approx 13.5$. The measurements at $Pe_r \approx 30$ are well into the regime where one may expect such an instability assuming Newtonian rheology. Additionally, the presence of the associated vortices would likely produce less significant alignment of the microstructure, leading to the observed deviations in the moments. It is therefore possible that the deviations at $Pe_r \approx 30$ are due to a Taylor instability. For the antisymmetric components of $\mathbf{S}^{(4)}$, the deviations of experiment from theory occur at Pe_r well below the expected onset of this instability.

Above $Pe_r = 1$, we find that the experimentally measured antisymmetric moments are significantly lower than what is predicted for a dilute suspension. We suggest that the differences in these components may be due to the presence of hydrodynamic and other interactions between rods. Importantly, it appears that the only effect such hydrodynamic interactions have is to modify the antisymmetric components of $\mathbf{S}^{(4)}$, while the other components of $\mathbf{S}^{(4)}$ are very similar to what is predicted by the dilute theory. We note further that the antisymmetric components of $\mathbf{S}^{(4)}$ are the three components

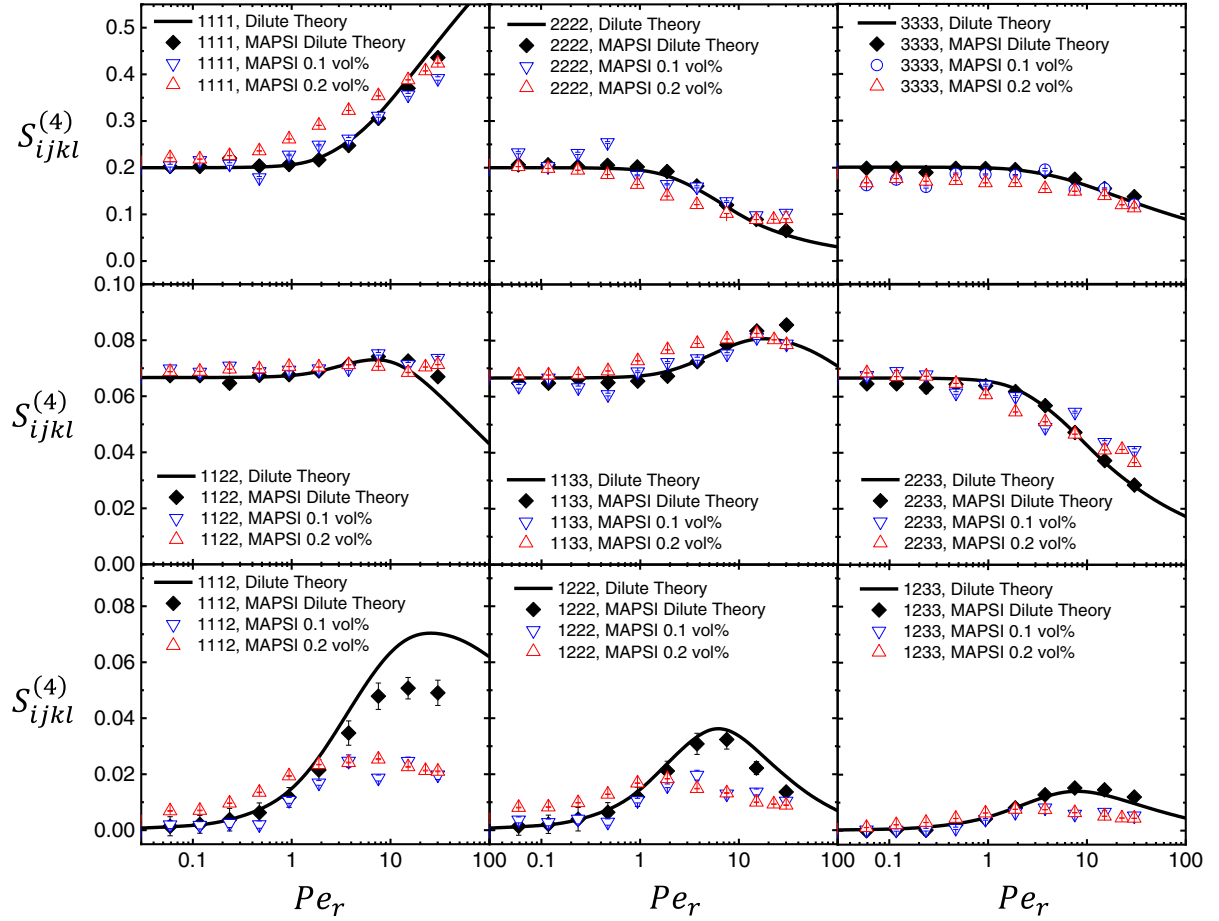


FIG. 8. Components of the fourth moment tensor, $S^{(4)}$ computed for the OPDFs extracted from MAPSI (points) compared to the dilute theory predictions (black lines) with varying Pe_r . The component of the moment tensor is indicated in the legend, where the four numbers correspond to the i, j, k , and l indices for the moment. Moments from SANS experiments with the fd-virus dispersion are indicated with the open circles while moments from SANS predictions from the dilute theory are indicated with the closed diamonds. The error bars indicate the standard deviation of the value from posterior sampling.

that contribute to S_{12} , which suggests that hydrodynamic interactions decreases this component of the second moment tensor, while other components are not significantly affected. Overall, a comparison of MAPSI extracted moments from experiment and the dilute suspension theory enable the quantification of the differences between the OPDFs.

D. Rheological characterization from scattering measurements

One important macroscopic property of the fd-virus dispersions is their rheological behavior. Here, we consider the behavior for the shear viscosity, and the two principle normal stress differences N_1 and N_2 , based on Batchelor's expression for the stress in noninteracting particle dispersions and using the experimentally measured second and fourth moments from the preceding section. These results are then compared to the dilute theory, the modified D-B model and, in the case of the shear stress, to values measured mechanically in a rheometer. The comparison to the dilute suspension theory provides a direct indication of the importance of particle interactions on the structure of the fd-virus dispersions. The comparison

with rheological measurements of the shear stress explicitly tests whether the stress expression for dilute systems due to Batchelor is accurate for this range of particle concentrations. Such an approach has previously been applied to studies of suspensions of spherical particles to estimate the particle contribution to the stress [66]. To our knowledge, this study is the first to utilize scattering measurements to directly estimate the particle contribution to the stress in elongated particle suspensions, here enabled by the ability to estimate the full OPDF of the material.

Figure 9 includes the rheological quantities as calculated from the SANS estimates of the moments and Batchelor's expression for the stress, compared to the dilute theory, to the modified D-B model and, in the case of the viscosity, to rheological measurements for the fd-virus dispersions. Figure 9(a) includes the particle contribution to the viscosity normalized by the solvent viscosity and volume fraction of particles, $\eta_p/\phi \eta_s$. The dilute theory (black line) predicts a constant viscosity at low shear rates and shear thinning behavior beyond $Pe_r = 1$ (i.e., $\dot{\gamma} = 17 \text{ s}^{-1}$). As mentioned

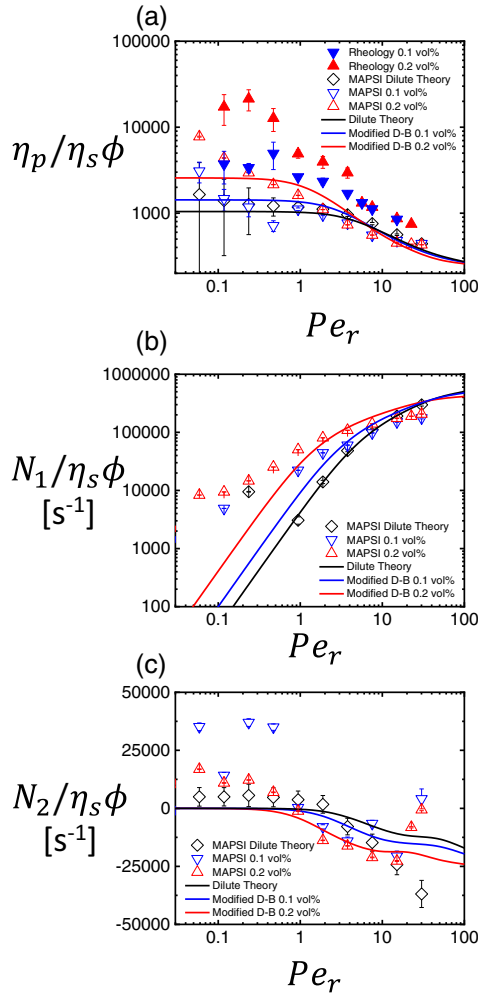


FIG. 9. Rheological quantities (a) the particle contribution to the viscosity, (b) the first normal stress difference, and (c) the second normal stress difference for the fd-virus dispersions in simple shear flow. The quantities are normalized by the solvent viscosity and the volume fraction of particles. The open symbols represent values determined using \mathbf{S} and $\mathbf{S}^{(4)}$ from MAPSI with Batchelor's expression for the stress tensor. The filled symbols are results from rheological measurements of the viscosity. The colors indicate the dispersion concentration including the dilute theory predictions of the scattering (black) and the measured 0.1 vol% (blue) and 0.2 vol% (red) fd-virus dispersions. Predictions from the dilute suspension theory are included as the solid black line. Predictions from the modified D-B model are included as the solid lines with colors corresponding to the concentrations of the measured points. The error bars represent the standard deviation of the measured quantity.

previously, the dilute theory prediction of $\eta_p/\eta_s\phi$ is independent of concentration. The colored lines are the predictions from the modified D-B model. Also included in this figure is $\eta_p/\eta_s\phi$ as determined from the SANS measurements and Batchelor's expression for the stress. For the 0.1 vol% dispersion, the value of $\eta_p/\eta_s\phi$ obtained in this way nearly matches that of the dilute theory for all shear rates. Furthermore, at this concentration the modified D-B model predictions are very close to those of the dilute theory. The exceptions are

at $Pe_r \approx 0.5$ and at moderate shear rates from $Pe_r \approx 4$ to 15 where the viscosity calculated from Batchelor's theory and moments inferred from SANS measurements is less than that predicted from the dilute theory. Compared to the 0.1 vol% dispersion, the 0.2 vol% dispersion shows similar behavior at high shear rates. However, at low shear rates, the predicted viscosities are greater than those of the 0.1 vol% dispersion, and, in addition, the 0.2 vol% dispersion shows shear thinning for all measured shear rates.

More striking, however, is that the rheological measurements of the shear viscosity for both the 0.1 vol% and 0.2 vol% dispersions produce values that are much greater even than the predictions from Batchelor's expression using the measured moments, especially at the lower shear rates. The 0.2 vol% dispersion again has a larger zero shear viscosity than the 0.1 vol% dispersion and again shear thins over the whole range of shear rates, whereas the onset of shear thinning in the 0.1 vol% dispersion is similar to the predictions from dilute theory as well as the values of calculated from Batchelor's theory and SANS measurements.

There are two additional observations worth mentioning. First, the data for the dilute case with the moments estimated from the theoretical scattering prediction via MAPSI are in quite close agreement with the dilute and modified D-B model predictions for low and moderate shear rates. Only for Pe_r values of order 10 or greater is there a difference between these two sets of results. A final interesting observation is that the values of $\eta_p/\eta_s\phi$ determined via the direct rheological measurements nearly collapse onto both the dilute theory prediction and the values calculated from Batchelor's theory and SANS measurements at the highest shear rates.

By comparing $\eta_p/\eta_s\phi$ determined from these various methods, we gain several key insights into the physical phenomena leading to the rheological response of fd-virus dispersions and, to the extent these results can be generalized, to other rodlike systems. Since the value of $\eta_p/\eta_s\phi$ calculated from MAPSI and Batchelor's expression is dependent on S_{12} and $S_{1122}^{(4)}$ and as was found in the previous section, the values of $S_{1122}^{(4)}$ remain nearly constant for the range of shear rates tested, the deviations in $\eta_p/\eta_s\phi$ between the 0.1 and 0.2 vol% dispersions are mainly a result of differences in the values of S_{12} . By comparing the values of $\eta_p/\eta_s\phi$ determined from SANS measurements, MAPSI and Batchelor's expression to those predicted from the dilute theory, we find that the measured contribution to $\eta_p/\eta_s\phi$ purely from particle alignment effects is different than that predicted by the dilute theory in two ways. Firstly, the dispersions at both concentrations have lower $\eta_p/\eta_s\phi$ than that predicted by the dilute theory at high shear rates, and the value of $\eta_p/\eta_s\phi$ at these high shear rates is independent of concentration. This result suggests that at high shear rates, the structure of the dispersions is independent of concentration, which was previously revealed in the analysis of \mathbf{S} and $\mathbf{S}^{(4)}$ in the previous section. Secondly, we find that at low shear rates the predictions obtained for the 0.1 vol% dispersion nearly match the dilute theory, while the 0.2 vol% dispersion has a SANS-determined viscosity nearly half an order of magnitude greater than the dilute theory. These two concentrations represent values slightly below (0.1 vol%) and above (0.2 vol%) the overlap concentration. Therefore, this

nonlinear effect is likely a result of interparticle interactions that become significant when particle lengths begin to overlap resulting in different values of S_{12} and, therefore, $\eta_p/\eta_s\phi$.

Finally, we compare $\eta_p/\eta_s\phi$ as measured with rheological measurements to those determined with SANS measurements, MAPSI and Batchelor's expression. At low shear rates, the rheological measurements of $\eta_p/\eta_s\phi$ are half an order of magnitude greater than those determined with SANS at both concentrations, suggesting that effects beyond simply the orientation of fd-viruses are contributing to the viscosity. However, at high shear rates, these values collapse onto one another, suggesting that whatever effects increase the low shear-rate viscosity are negligible at high shear rates. The most likely possibility for the difference in viscosity between the SANS predictions and the rheological measurements are the presence of direct (i.e., excluded volume) or indirect (i.e., hydrodynamic) particle-particle interactions. Given that the predictions based on Batchelor's expression collapse onto the measured viscosities at high shear rate, this suggests that effects from interparticle interactions are only significant at low shear rates and are negligible at high shear rates. The modified D-B theory suggests a contribution to $\eta_p/\eta_s\phi$ that is a function of the aspect ratio and volume fraction of particles. If we evaluate this extra contribution to the stress for the 0.1 vol% and 0.2 vol% dispersions we find that it results in a 25% and 45% increase in the zero-shear viscosity, respectively, which is much less than the observed increase by half an order of magnitude. A likely explanation for the discrepancy is that particle-particle interaction effects beyond excluded volume interactions contribute to the increased viscosity, although we do not have a reasonable explanation for what these effects may be at this time.

We turn to the normalized first normal stress difference, $N_1/\eta_s\phi$, which we compare between estimates from the SANS measurements on the fd-virus, the dilute and semidilute theories (which are again very similar), and the dilute (Batchelor) stress expression with moments determined via MAPSI [Fig. 9(b)]. Both the dilute theory and modified D-B model predict a monotonic increase in $N_1/\eta_s\phi$ with increasing shear rate. Although this monotonic increase is also observed for $N_1/\eta_s\phi$ estimated by SANS from both the 0.1 vol% and 0.2 vol% dispersions, the values of $N_1/\eta_s\phi$ are larger at low and moderate shear rates, and this deviation increases with the increase in concentration, similar to what was observed in the low shear-rate viscosity. This suggests that a concentration-dependent scaling of the shear rate (i.e., a concentration-dependent rotational diffusivity) could collapse the values of $N_1/\eta_s\phi$. For all shear rates, the higher concentration sample has a larger value of $N_1/\eta_s\phi$ for all shear rates, suggesting interparticle interactions are driving nonlinearities in the concentration dependence of the first normal stress difference.

Finally, for the normalized second normal stress difference, $N_2/\eta_s\phi$, the same set of results are shown in Fig. 9(c) as were just discussed for $N_1/\eta_s\phi$ in Fig. 9(b). The dilute theory and modified D-B model both predict a decreasing, negative $N_2/\eta_s\phi$ followed by a plateau value at $Pe_r \approx 10$ with increasing shear rate. Due to the measurement errors largely stemming from using only the flow-gradient and flow-vorticity measurement planes, the uncertainties on the values of $N_2/\eta_s\phi$ are much larger than for $\eta_p/\eta_s\phi$ or $N_1/\eta_s\phi$. How-

ever, to within this experimental uncertainty, the dispersions at both concentrations appear to have single particle contributions to the second normal stress differences that are reasonably well described by the dilute theory. We note a slight upturn in the average value of $N_2/\eta_s\phi$ at high shear rates, however due to the large error bars, we cannot conclusively comment on this feature. It is possible that this upturn is a result of a Taylor instability as was discussed in the previous section.

To summarize the findings of this section, we determined that MAPSI enables a novel comparison between theoretical structure-stress relationships for elongated particle dispersions and mechanical measurements of the stress. It was found that the "true" viscosity measured using rheometry was significantly larger than that determined by using the experimental measurements of the moments of the OPDF (from SANS measurements and MAPSI) and the Batchelor expression for the stress. Although it is clear that Batchelor's "dilute" expression for the stress is not adequate at the concentrations of the fd-virus suspensions, the modified Dhont-Briels model makes only a small correction to the dilute suspension theory at these concentrations, and does not account for the deviations we observe. A clear question remains as to the physics that lead to this increase in measured viscosity and the additional contributions to the stress due to particle interactions that may explain this result.

V. CONCLUSIONS

In this work, we presented a general framework to model SAS and extract anisotropic 3D orientation distributions for nonspherical particles aligned by an externally imposed field. For systems where the orientation distribution is known, we presented explicit expressions for the form factor (i.e., intraparticle scattering) for arbitrary particle shapes and orientation distributions. For systems where physical theories for predicting the full OPDF do not exist, we proposed a generalized Bayesian inference method, MAPSI, for inferring the OPDF from scattering data that relies only upon an orientation-dependent scattering model for the individual scattering object. Results from MAPSI using simulated scattering of dilute rod dispersions in shear flow were used to evaluate the inaccuracies incurred when various projections of the measured scattering and combinations thereof are used to extract the full 3D OPDF. We generally find that at least two projections of the scattering are required to extract accurate OPDFs. When only one scattering projection is used, the apparent OPDF broadens in the out-of-plane direction, owing to an inability to resolve the differences in scattering from particles oriented out-of-plane.

Next, the second and fourth moments of the OPDF were calculated from the extracted OPDFs to enable a quantitative comparison between OPDFs from SANS measurements and theory. The second and fourth moments were chosen as they represent a sufficient description of the OPDF for the calculation of mechanical properties of force-free dispersions of nonspherical particles, and therefore provide a clear route toward testing physical theories of such dispersions and structure-property relationships [12]. OPDFs extracted from measurements of a model rodlike particle dispersion at

concentrations near the overlap concentration were compared to the theory for dilute particles and the modified D-B model including mean-field hard rod interactions between particles. This comparison revealed deficiencies in the theoretical understanding of interparticle interactions between rods and quantified the aspects of the structural evolution of such dispersions that have yet to be understood.

Finally, the ability to extract moments of the OPDFs in combination with expressions relating the structure and stress for rodlike particle dispersions enables the direct estimation of rheological quantities based on components of the fluid stress. The extracted rheological quantities were compared to theory predictions and, in the case of the viscosity, rheological measurements. For the case of the viscosity, the comparison revealed that modern theories relating dispersion structure to stress significantly underpredict the stress contributions arising from interparticle interactions.

The methods proposed in this work enable quantitative extraction of the full 3D OPDF from SAS measurements, so long as an orientation-dependent particle scattering model can be derived. We speculate that the extension of MAPSI to include other distribution functions (e.g., particle size or shape distributions) may offer the ability to infer the structure of a much wider range of systems such as, for example, polydisperse or deformable systems where the different constituents or states of deformation, respectively, adopt distinct OPDFs. Overall, the ability to determine fourth moments of the OPDF directly from experimental data provides a powerful new tool for testing theoretical structure-property relations for anisotropic materials, and various closure approximations they rely upon [12,36,39,40,67,68]. We anticipate that the new tools provided by the current work will generate renewed interest and scrutiny of these theories.

ACKNOWLEDGMENTS

This material is based upon work supported by the U.S. Department of Energy, Office of Science, Office of Basic Energy Sciences under DE-SC0014127. K.S.S. was supported by the Department of Energy Computational Science Graduate Fellowship program under Grant No. DE-FG02-97ER25308. Preparation of samples was supported by NSF-DMR-1905384. C.L. and M.P.L. were funded by the European Union within the Horizon 2020 project under the DiStruc Marie Skłodowska Curie innovative training network; Grant Agreement No. 641839. We acknowledge the support of the National Institute of Standards and Technology, U.S. Department of Commerce, in providing the neutron research facilities used in this work. Access to VSANS was provided by the Center for High Resolution Neutron Scattering, a partnership between the National Institute of Standards and Technology and the National Science Foundation under Agreement No. DMR-1508249. This work benefited from the use of the SasView application, originally developed under NSF award DMR-0520547. SasView contains code developed with funding from the European Union's Horizon 2020 research and innovation programme under the SINE2020 project, Grant Agreement No. 654000.

APPENDIX A: FORWARD PREDICTION OF SAS FOR A DILUTE DISPERSION

With the scattering model for the fd-virus dispersions validated at equilibrium, we can compare SANS predictions from the combined scattering and orientational dynamics theory with SANS measurements of the fd-virus dispersion. We expect that the OPDF for the more dilute, 0.1 vol% dispersion can be somewhat described with the dilute rod theory, and we will compare these SANS predictions with no adjustable parameters to the experimentally measured SANS patterns for the 0.1 vol% dispersion.

Figures 10 and 11 include the results comparing the SANS from theory and experiment in the 1–3 and 1–2 planes respectively. We focus the comparison to 3 representative Pe_r (2, 7.5, and 30). The included shear rates range from the onset of discernable anisotropy in the SANS patterns to the highest measured shear rate. For these shear rates, we have included (i) the OPDF predicted from theory projected onto the surface of the unit sphere in the reference frame of the flow, (ii) the resulting SANS pattern predicted from the theory, (iii) the experimentally measured SANS pattern, and (iv) the absolute error or difference between these two patterns computed as $I_{\text{diff}}(\mathbf{q}) = |I_{\text{experiment}}(\mathbf{q}) - I_{\text{theory}}(\mathbf{q})|$.

For the 1–3 plane comparison (Fig. 10), we find excellent agreement when comparing the SANS patterns from the theory and experiments, both in the degree of anisotropy and the \mathbf{q} -range over which it occurs. The alignment of microstructure, which increases with increasing shear rate, produces SANS patterns with higher intensity in the vorticity direction (q_ω) and lower intensity in the flow direction (q_u) for a similar magnitude of \mathbf{q} . The onset of this discernable anisotropy in the SANS patterns occurs at $Pe_r \approx 2$. By analyzing the difference between the theory and experimental SANS patterns, we find that such deviations are isotropic and random for a majority of the \mathbf{q} -range probed. The exception to this is at the highest shear rate, $Pe_r \approx 30$, where we find larger differences between theory and experiment at low- \mathbf{q} and along the q_ω direction. We will discuss potential reasons for the increased errors at $Pe_r \approx 30$ later with the results from the 1–2 comparison.

For the 1–2 plane comparison (Fig. 11), we again find good agreement when comparing the SANS patterns from the theory and experiments. Like the 1–3 plane measurements, we begin to observe anisotropy in the SANS patterns at $Pe_r \approx 2$. Unlike the 1–3 plane measurements, the direction of minimum intensity (corresponding to the direction where most of the rods are aligned) shifts from 45° in the flow-gradient plane to 0° into the flow direction, in agreement with the theory-predicted OPDF. Indeed, the direction and magnitude of anisotropy in the scattering at high- q is captured well for all shear rates measured. For all measured \mathbf{q} , the differences between the theory and experiment are larger in the 1–2 than in the 1–3 measurements due to a larger standard deviation in the measured intensity. Larger systematic differences between theory and experiment are observed at low- q for the higher shear rates. In particular, we observe that the theory overpredicts the intensity along the direction of greatest anisotropy at the higher shear rates, and the magnitude of the overprediction increases with increasing shear rate.

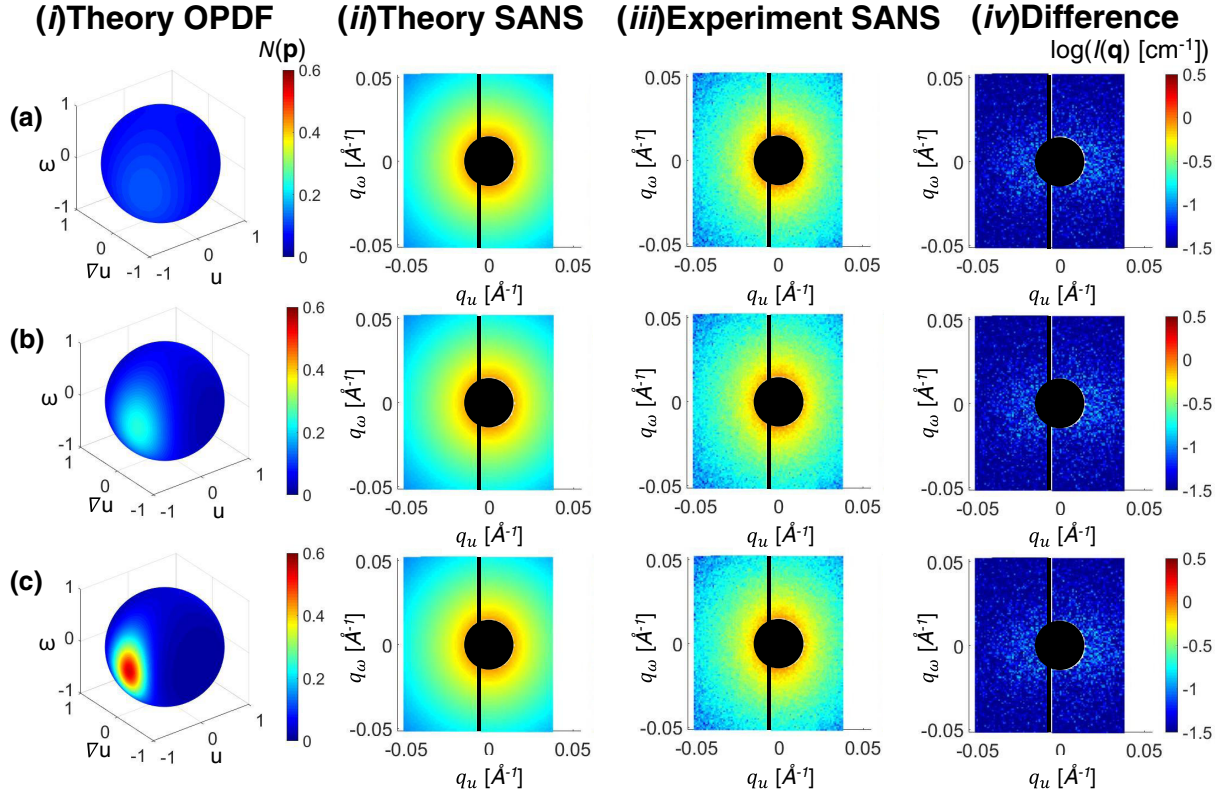


FIG. 10. Representative results of the 1–3 plane rheo-SANS experiments and theory predictions for Pe_r of approximately (a) 2, (b) 7.5, and (c) 30 corresponding to $\dot{\gamma} = 32, 128$, and 512 s^{-1} , respectively. Included are the (i) dilute theory predicted orientation distribution function (OPDF) relative to the real-space flow, gradient, and vorticity directions (u , ∇u , and ω , respectively), (ii) theoretically predicted SANS patterns, (iii) experimental SANS patterns, and (iv) difference between these two patterns. The intensities and differences for the 2D patterns are on logarithmic scales while the OPDFs are presented on a linear scale. The low- q cutoff and gap between detectors is indicated on the 2D patterns in black.

APPENDIX B: ASSESSMENT OF SCATTERING PARAMETERIZATION FOR EXTRACTING OPDFs

Despite the imperfect comparison between theory and experiment, we can use these results to assess the quality of information provided by previously-utilized analyses of anisotropic scattering based on a single 2D projection and its assumed relationship to the in-plane OPDF. To summarize the discussion in the introduction and the more detailed discussion in Ref. [15], one will typically either extract the annular variation of intensity with angle with respect to the detector, or calculate a scalar parameter characterizing the anisotropy based on the annular variation of intensity. Either of these methods is valid for assessing qualitative trends in particle alignment. However, these methods will be intrinsically convoluted by the fact that one is measuring a projection of the scattering onto a 2D plane. Furthermore, these methods discard useful information about the microstructure's OPDF that relies on the dependence of the intensity on the magnitude of \mathbf{q} , which is lost in the averaging. We will now assess whether such issues introduce systematic errors in the estimation of the OPDF from scalar parameterizations of the scattering anisotropy.

It is sometimes assumed that the annular variation in the scattering intensity is proportional to the in-plane projection of the OPDF shifted by π radians due to a

Fourier transform of the scattering intensity distribution, i.e., $I(\theta, q^*) = \alpha N(\theta - \pi, \phi = 0)$ for 1–3 plane measurements and $I(\phi, q^*) = \alpha N(\phi - \pi, \theta = \frac{\pi}{2})$ for 1–2 plane measurements, where $I(\theta, q^*)$ is the annular averaged scattering intensity in some q range, q^* , and α is a proportionality constant [13,23]. Alternatively, one can obtain a scalar parameterization of the annular variation by assuming that a simple relationship with the second moment of the in-plane OPDF exists (essentially assuming a similar equality between the scattering and in-plane OPDF as above). One such parameterization is the alignment factor (A_f), defined as

$$A_f(q^*) = -\frac{\int_0^{2\pi} I(\beta, q^*) \cos(2(\beta - \beta_0)) d\beta}{\int_0^{2\pi} I(\beta, q^*) d\beta}, \quad (\text{B1})$$

where β is the in-plane angle (i.e., θ or ϕ for 1–3 and 1–2 plane measurements respectively) and β_0 is the direction of most probable orientation. For measurements in the 1–3 plane, the alignment factor is sometimes assumed to be equal to S_m where $S_m = S_{11} - S_{33}$ for 1–3 plane measurements and $S_m = S_{11} - S_{22}$ for 1–2 plane measurements [25]. In other words, it is assumed that $A_f(q^*)$, as a scalar parameterization of the intensity, provides information about the corresponding second moment of the OPDF. While we only show results for this particular scalar parameterization of the intensity, we expect that the conclusions reached for $A_f(q^*)$ will be

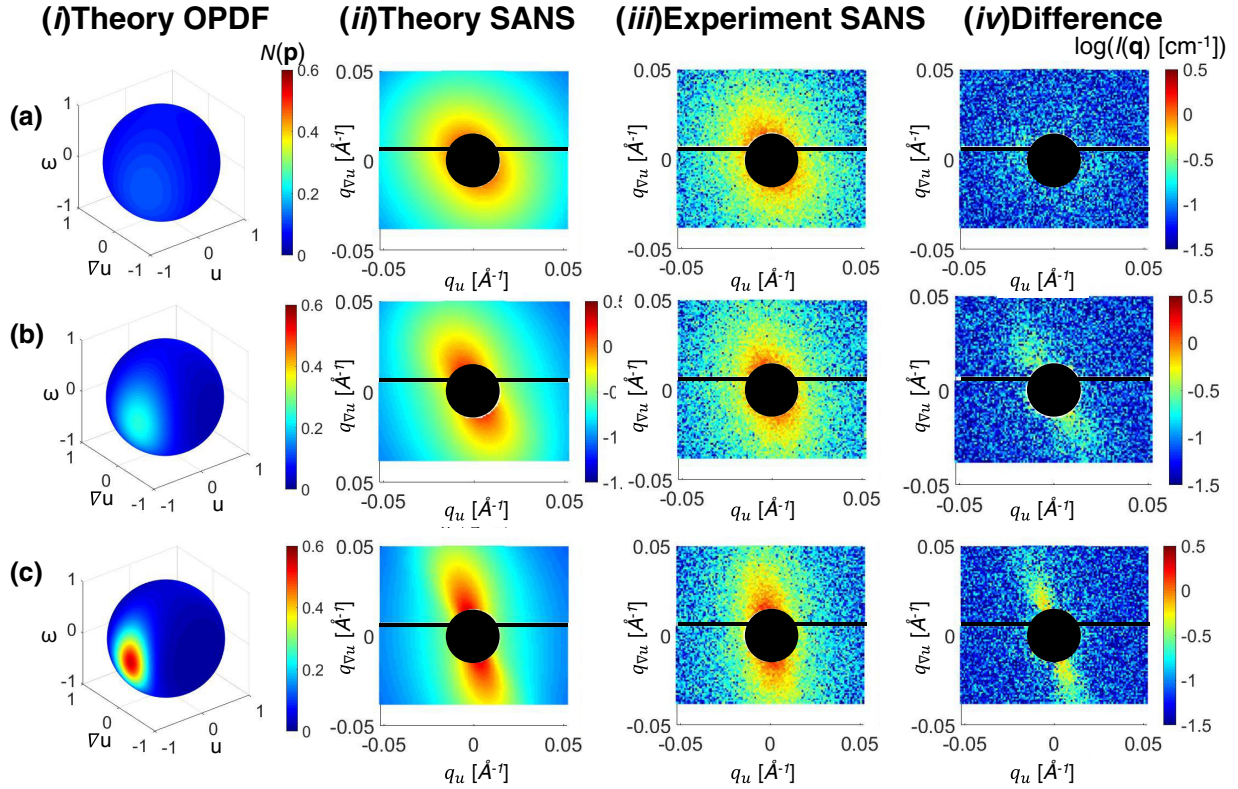


FIG. 11. Representative results of the 1–2 plane flow-SANS experiments and theory predictions for Pe_r of approximately (a) 2, (b) 7.5, and (c) 30 corresponding to $\dot{\gamma} = 32, 128$, and 512 s^{-1} , respectively. Included are the (i) dilute theory predicted orientation distribution function (OPDF) relative to the real-space flow, gradient, and vorticity directions (u , ∇u , and ω , respectively), (ii) theoretically predicted SANS patterns, (iii) experimental SANS patterns, and (iv) difference between these two patterns. The intensities and differences for the 2D patterns are on logarithmic scales while the OPDFs are presented on a linear scale. The low- q cutoff and gap between detectors is indicated on the 2D patterns in black.

independent of the precise scalar used (e.g., P_2 or Herman's orientation parameter).

For this study, we averaged the predicted scattering intensities over a q -range of 0.032 to 0.046 \AA^{-1} to match a previous study on fd-viruses [47]. Similar to this previous study, we find that only α is affected by the choice in q^* , so we did not consider the effect of changing q^* . Figures 12(a) and 12(b) include, for the 1–3 plane and 1–2 plane measurements respectively, a comparison of the experimentally measured annular averaged intensity (points), the theoretically predicted (solid lines) annular averaged intensity, and the in-plane projection of the actual OPDF (dotted lines) for the range of shear rates probed experimentally. As was found for the direct comparison of scattering intensity at all measured \mathbf{q} , we find excellent agreement between the experiments and the theoretical predictions for the annular averaged intensity. When comparing the annular averaged intensity (the solid lines) with the in-plane OPDF (the dotted lines), however, it is clear that one cannot assume that the annular averaged intensity provides a good approximation of the in-plane OPDF. Both produce similar qualitative trends: increasing shear rate leads to a more anisotropic variation in both the intensity and the in-plane OPDF. Furthermore, the direction of maximum alignment in the plane of measurement is consistent between the two curves. However, a quantitative proportionality

between the two does not hold. Clearly, estimates of the in-plane OPDF based upon the annular averaged intensity are subject to very significant error. Figures 12(c) and 12(d) include a comparison between the second moment of the OPDF (dotted line), the experimentally measured $A_f(q^*)$ (points) and the theoretically predicted $A_f(q^*)$ (solid line). As with the comparison of the annular variation in scattering intensity, we find that the qualitative trend in the second moment of the OPDF is properly captured by $A_f(q^*)$. Indeed, both metrics similarly capture regions of shear rate where the microstructure is not significantly aligned ($Pe_r < 1$) and where alignment is noticeable ($Pe_r > 1$). However, the values of $A_f(q^*)$ deviate quantitatively. Assuming a quantitative equality, or even proportionality, between $A_f(q^*)$ and S_m would lead one to experimentally underpredict the overall order in the system at high alignment, and overpredict the order at low alignment.

Taken together, these results suggest that there is a quantitative deviation in the presumed microstructural alignment when equating annular scattering intensity variations with the in-plane OPDF. Furthermore, no amount of proportional shifting of A_f will lead to quantitative agreement with the corresponding moment of the OPDF. We rationalize these results by noting that a proportionality between scattering intensity and OPDF intrinsically requires that the scattering amplitude is a delta function of intensity in the orientation direction,

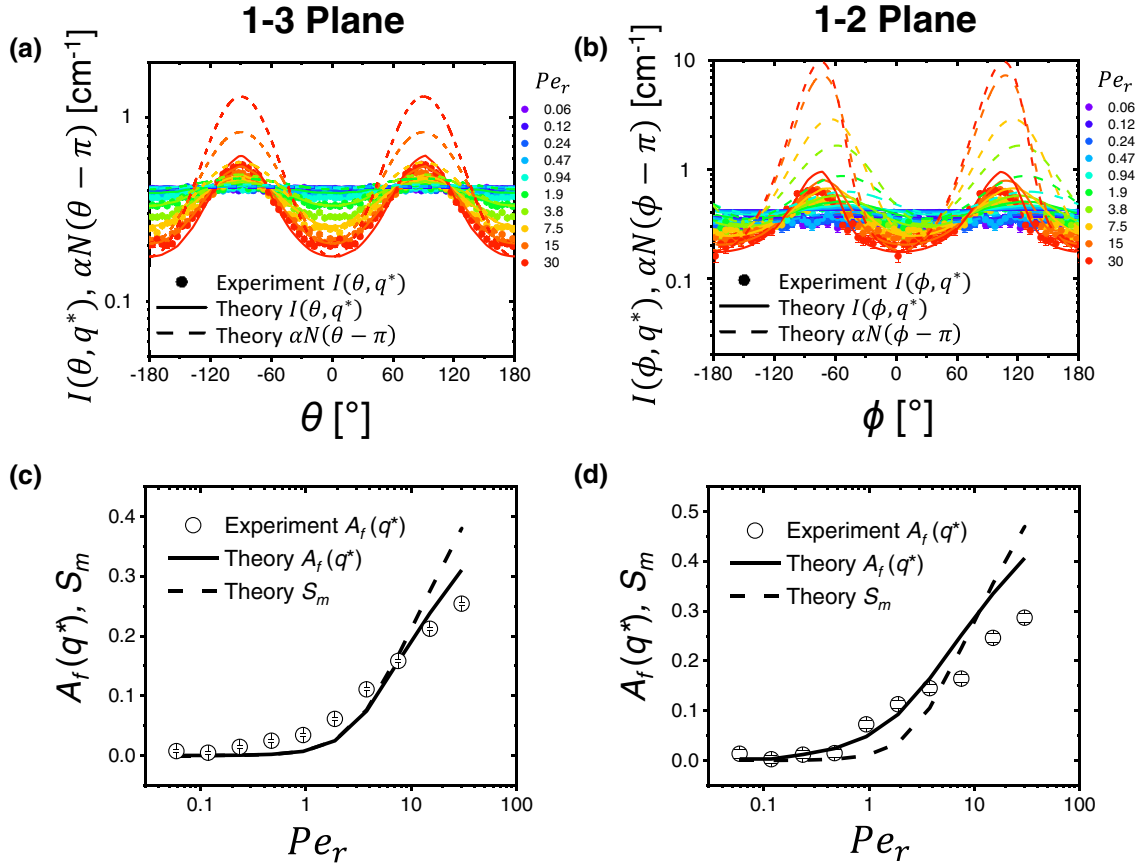


FIG. 12. (a) Averaged scattering intensity, $I(\theta, q^*)$, as a function of annular angle θ within a q -range of 0.032 and 0.046 \AA^{-1} for the 1–3 plane. (b) Averaged scattering intensity, $I(\phi, q^*)$, as a function of annular angle ϕ within a q -range of 0.032 and 0.046 \AA^{-1} for the 1–2 plane. For (a) and (b), the colored points correspond to experimentally measured intensity for Pe_r from 0.06 to 30 (purple to red), which corresponds to shear rates from 1 to 512 s^{-1} . The solid colored lines correspond to the theoretically predicted average scattering intensity at conditions matching the experiments. The dotted colored lines are the in plane OPDF from the theory (i.e., $\phi = 0$ or $\theta = \frac{\pi}{2}$ for the 1–3 and 1–2 planes, respectively). The value of α was chosen for each shear rate to have the value of $\alpha N(\theta - \pi)$ equal $I(\theta, q^*)$ or $\alpha N(\phi - \pi)$ equal $I(\phi, q^*)$ at the minimum intensity. (c) and (d) Alignment factor ($A_f(q^*)$) as a function of shear rate for the experimentally measured scattering (solid points) and scattering predicted from the dilute rod theory (solid line). Included on the same plot (dotted line) is $S_m = S_{11} - S_{33}$ or $S_m = S_{11} - S_{22}$ for the 1–3 and 1–2 planes, respectively, from the OPDF simulation.

regardless of the microstructure's out-of-plane orientation. In reality, the scattering amplitude (in this case, the form factor) is a continuous function that depends on the out-of-plane orientation. The fact that the function is continuous means that the intensity contribution from a perfectly aligned microstructure will be spread out over an annular range, leading to less anisotropy in the scattering intensity variation than in the OPDF. It is possible that for distributions that are uniaxial or with uniform probability in the out-of-plane direction, such

a relationship will be found to hold more precisely. However, in general, any parameterization of anisotropic scattering will potentially depend on the scattering model employed, the q range used for the calculation, the q discretization in the experiment and the degree to which the microstructure is oriented out-of-plane. We conclude that one should not expect a moment parameterization of the anisotropic scattering to be directly proportional to the corresponding moment of the OPDF.

- [1] R. B. Bird, R. C. Armstrong, and O. Hassager, *Dynamics of Polymeric Liquids* (Wiley, New York, 1987).
- [2] R. G. Larson, *The Structure and Rheology of Complex Fluids* (Oxford University Press, 1999).
- [3] T. Zemb and P. Lindner, *Neutron, X-Rays and Light. Scattering Methods Applied to Soft Condensed Matter* (North Holland, 2002).
- [4] A. P. R. Eberle and L. Porcar, *Curr. Opin. Colloid Interface Sci.* **17**, 33 (2012).
- [5] P. T. Corona, N. Ruocco, K. M. Weigandt, L. G. Leal, and M. E. Helgeson, *Sci. Rep.* **8**, 15559 (2018).
- [6] A. Bharati, S. D. Hudson, and K. M. Weigandt, *Curr. Opin. Colloid Interface Sci.* **42**, 137 (2019).
- [7] P. W. Majewski, M. Gopinadhan, and C. O. Osuji, *J. Polym. Sci. Part B Polym. Phys.* **50**, 2 (2012).
- [8] H. Löwen, *J. Phys.: Condens. Matter* **20**, 404201 (2008).
- [9] M. E. Helgeson, P. A. Vasquez, E. W. Kaler, and N. J. Wagner, *J. Rheol.* **53**, 727 (2009).

- [10] S. A. Rogers and M. P. Lettinga, *J. Rheol.* **56**, 1 (2012).
- [11] J. C.-W. Lee, K. M. Weigandt, E. G. Kelley, and S. A. Rogers, *Phys. Rev. Lett.* **122**, 248003 (2019).
- [12] G. K. Batchelor, *J. Fluid Mech.* **41**, 545 (1970).
- [13] P. Davidson, D. Petermann, and A. M. Levelut, *J. Phys. II France* **5**, 113 (1995).
- [14] G. Huang, Y. Wang, C. Do, Y. Shinohara, T. Egami, L. Porcar, Y. Liu, and W.-R. Chen, *ACS Macro Lett.* **8**, 1257 (2019).
- [15] See Supplemental Material at <http://link.aps.org/supplemental/10.1103/PhysRevMaterials.5.065601> for more information including a generalization of the calculation of form factor scattering for arbitrarily oriented particles, a review of methods for analyzing anisotropic SAS from soft materials, a summary of rheological theories for suspensions of Brownian particles and a more in-depth overview of MAPSI, which includes Refs. [69–78].
- [16] C. Burger, B. S. Hsiao, and B. Chu, *Polym. Rev.* **50**, 91 (2010).
- [17] G. R. Huang, Y. Wang, B. Wu, Z. Wang, C. Do, G. S. Smith, W. Bras, L. Porcar, P. Falus, and W. R. Chen, *Phys. Rev. E* **96**, 022612 (2017).
- [18] G. R. Huang, Y. Wang, C. Do, L. Porcar, Y. Shinohara, T. Egami, and W. R. Chen, *J. Phys. Chem. Lett.* **10**, 3978 (2019).
- [19] M. Liebi, M. Georgiadis, A. Menzel, P. Schneider, J. Kohlbrecher, O. Bunk, and M. Guizar-Sicairos, *Nature* **527**, 349 (2015).
- [20] L. Porcar, D. Pozzo, G. Langenbucher, J. Moyer, and P. D. Butler, *Rev. Sci. Instrum.* **82**, 083902 (2011).
- [21] A. K. Gurnon, P. D. Godfrin, N. J. Wagner, A. P. R. Eberle, P. Butler, and L. Porcar, *J. Vis. Exp.* **84**, e51068 (2014).
- [22] P. H. Hermans, J. J. Hermans, D. Vermaas, and A. Weidinger, *J. Polym. Sci.* **2**, 632 (1947).
- [23] A. J. Leadbetter and E. K. Norris, *Mol. Phys.* **38**, 669 (1979).
- [24] S. V. Savenko and M. Dijkstra, *Phys. Rev. E* **70**, 011705 (2004).
- [25] T. Rosén, C. Brouzet, S. V. Roth, F. Lundell, and L. D. Söderberg, *J. Phys. Chem. C* **122**, 6889 (2018).
- [26] L. M. Walker and N. J. Wagner, *Macromolecules* **29**, 2298 (1996).
- [27] K. R. Purdy, Z. Dogic, S. Fraden, A. Rühm, L. Lurio, and S. G. J. Mochrie, *Phys. Rev. E* **67**, 031708 (2003).
- [28] J. B. Hayter and J. Penfold, *J. Phys. Chem.* **88**, 4589 (1984).
- [29] L. Herbst, J. Kalus, R. P. P. May, H. Hoffmann, K. Ibel, H. Thurn, J. Kalus, H. Thurn, K. Ibel, and R. P. P. May, *Chem. Phys.* **103**, 437 (1985).
- [30] P. G. Cummins, E. Staples, J. B. Hayter, and J. Penfold, *J. Chem. Soc. Faraday Trans. 1 Phys. Chem. Condens. Phases* **83**, 2773 (1987).
- [31] J. Kalus, H. Hoffmann, and K. Ibel, *Colloid Polym. Sci.* **267**, 818 (1989).
- [32] J. Penfold, E. Staples, and P. G. Cummins, in *Am. Chem. Soc. Polym. Prepr. Div. Polym. Chem.* (1990), p. 98, https://inis.iaea.org/search/search.aspx?orig_q=RN:23081406.
- [33] E. Helfer, P. Panine, M. F. Carlier, and P. Davidson, *Biophys. J.* **89**, 543 (2005).
- [34] K. M. Weigandt, L. Porcar, and D. C. Pozzo, *Soft Matter* **7**, 9992 (2011).
- [35] S. Förster, M. Konrad, and P. Lindner, *Phys. Rev. Lett.* **94**, 017803 (2005).
- [36] E. J. Hinch and L. G. Leal, *J. Fluid Mech.* **76**, 187 (1976).
- [37] G. B. Jeffery, *Proc. R. Soc. A Math. Phys. Eng. Sci.* **102**, 161 (1922).
- [38] N. Kuzuu and M. Doi, *J. Phys. Soc. Jpn.* **52**, 3486 (1983).
- [39] J. K. G. G. Dhont and W. J. Briels, *Colloids Surfaces A Physicochem. Eng. Asp.* **213**, 131 (2003).
- [40] C. Lang, J. Kohlbrecher, L. Porcar, A. Radulescu, K. Sellinghoff, J. K. G. Dhont, and M. P. Lettinga, *Macromolecules* **52**, 9604 (2019).
- [41] G. J. Ennis, A. Okagawa, and S. G. Mason, *Can. J. Chem.* **56**, 2824 (1978).
- [42] I. Kirchenbuechler, D. Guu, N. A. Kurniawan, G. H. Koenderink, and M. P. Lettinga, *Nat. Commun.* **5**, 5060 (2014).
- [43] D. Kumar, A. Shenoy, S. Li, and C. M. Schroeder, *Phys. Rev. Fluids* **4**, 114203 (2019).
- [44] M. P. Lettinga and J. K. G. Dhont, *J. Phys.: Condens. Matter* **16**, S3929 (2004).
- [45] M. P. Lettinga, Z. Dogic, H. Wang, and J. Vermant, *Langmuir* **21**, 8048 (2005).
- [46] E. Barry, D. Beller, and Z. Dogic, *Soft Matter* **5**, 2563 (2009).
- [47] C. Lang, J. Kohlbrecher, L. Porcar, and M. P. Lettinga, *Polymers (Basel)* **8**, 291 (2016).
- [48] C. Lang, J. Hendricks, Z. Zhang, N. K. Reddy, J. P. Rothstein, M. P. Lettinga, J. Vermant, and C. Clasen, *Soft Matter* **15**, 833 (2019).
- [49] T. Maniatis, J. Sambrook, and E. Fritsch, *Molecular Cloning* (Cold Spring Harbor Univ. Press, New York, 1989).
- [50] S. R. Kline, *J. Appl. Crystallogr.* **39**, 895 (2006).
- [51] H. Brenner, *Int. J. Multiph. Flow* **1**, 195 (1974).
- [52] L. G. Leal and E. J. Hinch, *Rheol. Acta* **12**, 127 (1973).
- [53] G. K. Batchelor, *J. Fluid Mech.* **44**, 419 (1970).
- [54] J. Férec, M. Heniche, M. C. Heuzey, G. Ausias, and P. J. Carreau, *J. Non-Newtonian Fluid Mech.* **155**, 20 (2008).
- [55] F. Folgar and C. L. Tucker, *J. Reinf. Plast. Compos.* **3**, 98 (1984).
- [56] M. Doi and S. F. Edwards, *J. Chem. Soc. Faraday Trans. 2 Mol. Chem. Phys.* **74**, 560 (1978).
- [57] C. Lang and M. P. Lettinga, *Macromolecules* **53**, 2662 (2020).
- [58] M. Doucet, J. H. Cho, G. Alina, S. King, P. Butler, P. Kienzle, P. Parker, J. Krzywon, A. Jackson, T. Richter, M. Gonzales, T. Nielsen, R. Ferraz Leal, A. Markvardsen, R. Heenan, P. Juhas, and J. Bakker, SasView version 3.1.2 (Version v3.1.2), Zenodo (9 December 2015), <http://doi.org/10.5281/zenodo.35065>.
- [59] B. Weyerich, J. Brunner-Popela, and O. Glatter, *J. Appl. Crystallogr.* **32**, 197 (1999).
- [60] A. T. Holmes, *Phys. Rev. B* **90**, 024514 (2014).
- [61] R. T. C. Ju, C. W. Frank, and A. P. Gast, *Langmuir* **8**, 2165 (1992).
- [62] C. W. Groetsch, *The Theory of Tikhonov Regularization for Fredholm Equations of the First Kind* (Pitman Advanced Pub. Program, Boston, 1984).
- [63] K. S. Silmore, X. Gong, M. S. Strano, and J. W. Swan, *ACS Nano* **13**, 3940 (2019).
- [64] Y. Y. Kurihara and J. L. Holloway, *Mon. Weather Rev.* **95**, 509 (1967).
- [65] Y. A. Wang, X. Yu, S. Overman, M. Tsuboi, G. J. Thomas, and E. H. Egelman, *J. Mol. Biol.* **361**, 209 (2006).
- [66] A. K. K. Gurnon and N. J. Wagner, *J. Fluid Mech.* **769**, 242 (2015).
- [67] J. J. Feng, G. Sgalari, and L. G. Leal, *J. Rheol.* **44**, 1085 (2000).

- [68] S. Dutta and M. D. Graham, *J. Non-Newtonian Fluid Mech.* **251**, 97 (2018).
- [69] M. E. Helgeson, M. D. Reichert, Y. T. Hu, and N. J. Wagner, *Soft Matter* **5**, 3858 (2009).
- [70] Z. Wang, C. N. Lam, W. R. Chen, W. Wang, J. Liu, Y. Liu, L. Porcar, C. B. Stanley, Z. Zhao, K. Hong, and Y. Wang, *Phys. Rev. X* **7**, 031003 (2017).
- [71] R. S. Bay, Fiber orientation in injection-molded composites: A comparison of theory and experiment, Ph.D. thesis, University of Illinois at Urbana-Champaign, 1991.
- [72] E. J. Hinch and L. G. Leal, *J. Fluid Mech.* **57**, 753 (1973).
- [73] M. Doi and S. Edwards, *The Theory of Polymer Dynamics* (Oxford University Press, New York, 1986).
- [74] W. Maier and A. Saupe, *Z. Naturforsch.* **13**, 564 (1958).
- [75] M. E. Rognes, D. A. Ham, C. J. Cotter, and A. T. T. McRae, *Geosci. Model Dev.* **6**, 2099 (2013).
- [76] K. Atkinson, *J. Aust. Math. Soc. Ser. B. Appl. Math.* **23**, 332 (1982).
- [77] A. Townsend, H. Wilber, and G. B. Wright, *SIAM J. Sci. Comput.* **38**, C403 (2016).
- [78] T. A. Driscoll, N. Hale, and L. N. Trefethen (eds.), *Chebfun Guide* (Pafnuty Publications, Oxford, 2014).